Cross-Measurement Comparisons for a CFD Validation Dataset on Mach 2.5 Axisymmetric Turbulent Shock-Wave/Boundary-Layer Interactions

Heath H. Reising*
NASA Glenn Research Center, Cleveland, OH, 44135

Jonathan Sasson†
Airbus U.S. Space & Defense, Merritt Island, FL, 32953

David O. Davis*, David J. Friedlander*, and Layton W. Howerton‡
NASA Glenn Research Center, Cleveland, OH, 44135

Experimental data for a shock-wave/boundary-layer interaction has been collected using multiple measurement techniques. Unfortunately, diversity of methods for acquisition begets an aggregation of data which does not directly quantify the same properties of the flowfield. The objective in this paper was to (a) present the collection of flowfield measurements in one venue in a format more usable for those validating CFD models against the data, (b) evaluate the degree to which the experimental data support each other, and (c) highlight the differences and relative advantages/shortcomings of each measurement techniques. To present the various measured quantities into common format, CFD results from a companion paper also submitted for presentation at this meeting are utilized. For the case where the boundary layer remains attached, there is agreement between the various measurements as well as with Reynolds-averaged Navier-Stokes simulation solutions. As the impinging shock strength is increased beyond the point of separating the boundary layer, the congruity of the data wanes. Generally, agreement among the measurements exceeds the degree to which the CFD solutions agree with experiments. This suggests that unmodeled physical phenomena, such as transient motion of the reflected shock and separation bubble, give rise to the discrepancies observed in the computational results.

Nomenclature

E = hot-wire anemometer voltage
k = turbulent kinetic energy, $\frac{1}{2}\overline{u_i' u_i'}$
M = Mach number
P = pressure
R = test section radius, 8.5 cm
Re_D = core flow Reynolds number based on test section hydraulic diameter ($2R$)
S = hot-wire senstivity coefficient
T = temperature
$\vec{U}$ = velocity vector (U, V, W)
U = axial velocity (aligned with $\vec{x}$)
V = vertical velocity (aligned with $\vec{y}$)
W = spanwise velocity (aligned with $\vec{z}$)
x = axial coordinate, $x = 0$ at leading edge of test section
y = vertical coordinate, $y = 0$ on test section axis
$\overline{y}$ = wall-normal coordinate, $\overline{y} = 0$ at $(r, \theta) = (R, \theta)$

*Aerospace Engineer, Inlets and Nozzles Branch, 21000 Brookpark Rd M/S 5-12, AIAA Senior Member.
†Sr. Mechanical Thermal Engineer, AIAA Senior Member.
‡Aerospace Engineer, Inlets and Nozzles Branch, 21000 Brookpark Rd M/S 5-12, AIAA Student Member.

z = spanwise coordinate, $z = 0$ on test section axis
α = shock generator cone half-angle
δ^* = boundary layer displacement thickness
θ = boundary layer momentum thickness or azimuth in cylindrical coordinate system, $\theta = 0$ at 12 o'clock and is clockwise positive looking upstream
ρ = density
τ^t_{ij} = turbulent (Reynolds) stress tensor
τ_{ij} = viscous stress tensor

Subscripts

i = inviscid shock impingement
p = Pitot
r = recovery
t = total condition or turbulent condition
w = wall condition
0 = facility nozzle exit station
1 = station at which incoming boundary layer is evaluated
∞ = freestream or boundary layer edge condition

Special Notations

$\overline{(\quad)}$ = time average (Reynolds average)
$\widetilde{(\quad)}$ = density-weighted time average (Favre average)
$(\quad)'$ = Reynolds fluctuation
$(\quad)''$ = Favre fluctuation

I. Introduction

Validation of turbulence models is paramount in the pursuit of accurate computational fluid dynamics (CFD) predictions in the complex flowfields present in realistic aerospace vehicles and propulsion systems. Typically, methods which rely on modeling of the turbulent flow physics (e.g., Reynolds stresses and heat flux vector in Reynolds-averaged Navier-Stokes (RANS) simulations) are less computationally expensive and can be used in parametric optimization studies. However, the models used within these lower-fidelity methods are almost universally calibrated in equilibrium turbulence and require careful tuning to accurately predict the production, transport, and dissipation of turbulence in complex flowfields. Shock-wave/boundary-layer interactions are typically identified as a problematic case for RANS solvers due to their large departure from an equilibrium turbulence state [1].

A dearth of high quality experimental data in supersonic and hypersonic shock-wave/boundary-layer interactions for use in code validation efforts was identified by Settles and Dodson [2]. There, many of the candidate datasets were rejected due to the lack of well-defined boundary conditions, undocumented 3D effects, inconsistency between repeated measurements, or a lack of repeated measurements. A specific methodology was laid out in Ref. 3 for planning useful CFD code validation experiments which acknowledges the interdependency between the requirements and capabilities of experimental and computational results.

In addition to the overall lack of high-quality experimental data, the influence of the glancing sidewall interaction is commingled with many nominally 2D SWBLI datasets. References 4 and 5 show only two of many examples where blockage generated by corner separations influence the strength of the primary SWBLI. Thus, the current campaign aims to use an axisymmetric wind tunnel test section and shock generator cone to circumvent this issue.

The Turbulent Computation Fluid Dynamics Validation Experiment (TCFDVE) has been an ongoing effort funded by the Transformation Tools and Technologies (TTT) project at NASA Glenn Research Center (GRC) to provide a high-quality experimental dataset of a SWBLI which is free of sidewall effects. A key component of a high-quality CFD validation dataset is the corroboration of a multitude of independent redundant measurements. This report presents flowfield data from the various measurement techniques applied in this campaign.

II. Apparatus and Procedure

A schematic of the flowfield being studied is shown in Fig. 1. Simple cone-cylinder bodies were used to generate the initial shock wave which impinges on the naturally-growing test section boundary layer. This provides a relatively thick profile in which to perform the detailed measurements required. The cone half-angle, α, was varied to provide both unseparated and separated interactions.

Figure 1 also gives a pictorial reference for the coordinate system and nomenclature used throughout this paper. Spatial coordinate are shown in both Cartesian (gray) and cylindrical (blue) systems to connect between the measurements and the axisymmetric geometry. While x is indicated to reference from the test section leading edge, the data is generally presented relative to the location of the inviscid shock impingement station. The directions for the defined velocity components which align with the typical convention for Cartesian coordinates are represented in green.

The various flowfield measurement techniques applied in this campaign each have advantages and drawbacks. The intent of this paper is to make direct comparisons between them, where possible, to elucidate the differences and unify the measurements into a consensus on the flowfield behavior for CFD validation efforts.

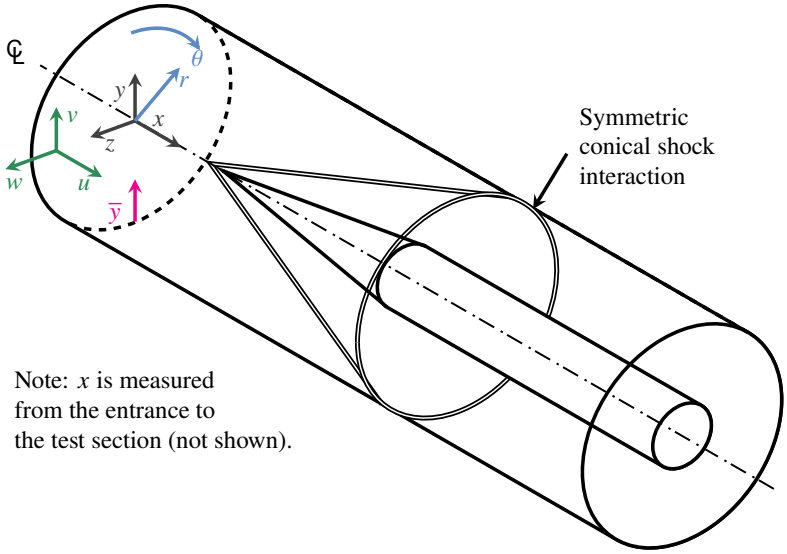


Fig. 1 Basic geometry and coordinate systems.

A. Test Facility

For the test results presented herein, the tunnel was configured with its axisymmetric 17 cm diameter test section and a Mach 2.5 converging-diverging nozzle. The wind tunnel and the specific test section geometry used for this test has been described thoroughly in Refs. 6–9.

The cone-cylinder centerbodies used to generate the impinging shock waves were highly configurable. Three tip cone half-angles were available to generate interactions of various strengths: 10° for an unseparated interaction, 13.5° for incipient separation, and 16° for a fully separated interaction. The cylindrical portion of the body was 5 cm in diameter and was comprised of a collection of spacer pieces to generate the desired axial length. A specific length of spacer stack was selected for each cone angle to place the inviscid impingement at the same axial station as in Ref. 7. The cone-cylinders were cantilevered from a support strut spanning the aft end of the section. This strut had a sharp leading edge to reduce blockage and, thus, lower the minimum Reynolds number condition available for testing. Three mounting positions were available on the strut. A centerline position allows for the generation of an axisymmetric interaction as shown in Fig. 1, while two offset positions generate swept interactions. For the TCFDVE campaign, the near-wall measurements were made at the $\theta = 180°$ position. Thus, a secondary vertical coordinate, $\bar{y} = R - r$, is defined (magenta in Fig. 1) which aligns the presented data with typical wall-referenced coordinates used when presenting boundary layer data.

The axisymmetric case requires sampling only in one x-r plane to fully describe the flowfield. As will be described in Section II.B, the probe-based measurements took advantage of this feature to reduce the reach required for the

probe mount and traversing apparatus. Likewise, this enabled the application of particle image velocimetry (PIV) measurements in this facility using a fixed laser sheet position and a local seeding technique. Due to the strong local flow angularity (see Ref. 9), the PIV technique was the only flowfield measurement applied in the swept interactions. Due to the resulting lack of redundant flowfield measurements in the swept interactions, only the axisymmetric configurations are analyzed herein.

B. Flowfield Measurement Techniques

Pitot probe measurements quantify the total pressure of the flowfield at the probe face. In supersonic flow, this measured pressure is aft of the bow shock which forms due to the presence of the probe. At the high Reynolds number and relatively small scale of the current experiments, all measurements are made in supersonic flow, except for the separated region. Both the total pressure loss across the bow shock and the resulting downstream Mach number are unique functions of the local undisturbed Mach number and thus, the measurement can be related to the undisturbed stagnation pressure of the flow with knowledge of the pressure of the undisturbed flow.

The Pitot probe geometry and pressure measurement system are described in Ref. 7. In summary, the probe tip was 0.63 mm in diameter with 0.15 mm walls. The probe was traversed in the y-z plane using a pair of screw-driven positioning stages which are actuated by stepper motors. This precision system uses feedback from digital encoders to locate the probe tip. The exact location of the wall is established by sensing electrical continuity between the probe and test section.

Hot-wire measurements provide a more direct measurement of the kinematic behavior of the flow. The measurement is sensitive to heat transfer between the thin metallic wire and the gas flow, which yields information about the local mass flux and temperature. For very thin wires (3-5 um), operated with appropriate anemometry electronics, a flat frequency response out to approximately 100 kHz can be obtained. This can be used to make inferences about the dynamic behavior of the flow in both the incoming turbulent boundary layer and its interaction with the impinging shock wave.

Hot-wire probes used in this experiment are described in great detail in [7]. In summary, the sensing element is a 5 µm diameter platinum-coated tungsten wire which is soldered to a streamlined probe (TSI Model 1214) to give a length-to-diameter ratio of approximately 200. The hot-wire measurements used the same traversing system as the Pitot probes to survey the flow. The probe signal was operated with a constant-voltage anemometer (CVA), which has superior bandwidth, signal-to-noise, and insensitivity to cable effects compared to other anemometer designs [10]. The data was low-pass filtered at 64 kHz and acquired by the facility data system at 200 kHz.

Particle image velocimetry was also applied in this series of experiments. By introducing tracer particles into the flowfield, illuminating them with a laser sheet, and capturing image pairs of the particle locations in rapid succession, the PIV technique captures velocity data simultaneously over a finite range of the flowfield. This method does not induce the probe effects of the previous two techniques, but necessitates the introduction of optical access for camera(s) to view the flowfield of interest. Additionally, the fundamental principles of this technique require that the tracers faithfully follow the underlying gas flow, which requires careful consideration in high-speed and rarefied flows.

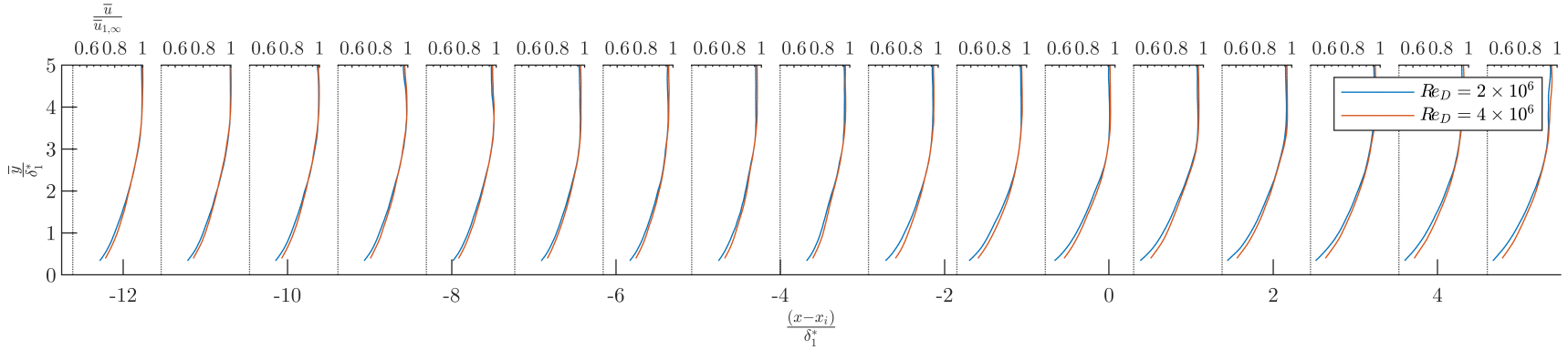
Development of the PIV seeding system was presented in Ref. 11. The apparatus for forming the laser sheet and introducing it into the wind tunnel as well as detailed information on the camera positioning for stereoscopic measurement are described in Ref. 9. In summary, the PIV system utilized a laser sheet which covered $\overline{y}$ of 0–30 mm with a thickness of approximately 1 mm in the measurement region. The viewing angles necessitated by the requirement of inducing minimal flow disturbance at the viewing windows produce a downward-looking view of the laser sheet which is suboptimal for near-wall measurements. This results in a minimum wall-normal distance of 1 mm for valid velocity data. Additionally, although great care was taken to produce a laser sheet which was parallel to the test section axis, any amount of seed material on the wall results in a bright burst of scattering near the wall which precludes capturing valid data in that region. The average magnification within the measurement region resulted in a scaling of 65 $\frac{\text{pix}}{\text{mm}}$, which results in a freestream displacement of approximately 18.5 pix for the 0.5 µs inter-pulse time used for the entirety of the campaign.

C. Test Parameters

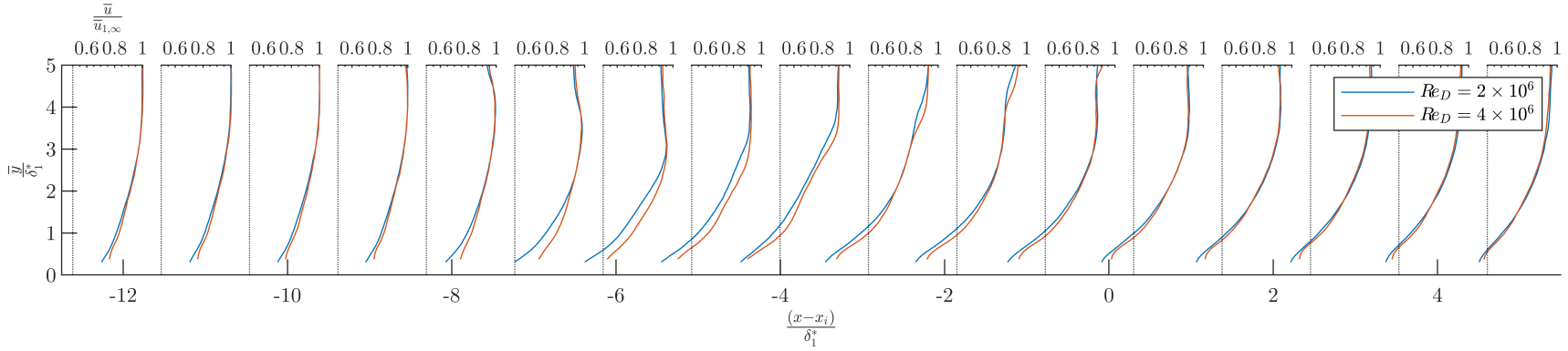
Previous publication of detailed PIV results [9] focused on $Re_D = 2 \times 10^6$ due to the favorable scale of the boundary layer relative to the measurement spatial resolution and the reduced grid requirements for scale-resolving simulations [9]. However, a great majority of the probe data was collected at $Re_D = 4 \times 10^6$ [7, 8]. Since PIV data was taken at both conditions, comparisons can be made between the data at the two conditions. Figures 2 and 3 show the mean and turbulent streamwise velocity behavior at these two Reynolds number conditions for both the $\alpha = 10°$ (weak) and $\alpha = 16°$ (strong) SWBLIs. The interaction with a weaker impinging shock shows little change as the Reynolds number is varied if the data is normalized such that the difference in boundary layer scales is removed. The $\alpha = 16°$ case exhibits some difference in the behavior due to an increased upstream influence at lower Reynolds number. This is visible in both the mean velocity and axial turbulence data, where the profiles begin to deviate from the incoming boundary layer behavior at the fifth station ($x = 469.9$ mm). However, the effect dissipates with downstream distance and both quantities approach the same profile downstream of the interaction.

A summary chart visualizing the spatial locations of the various flowfield measurements is presented schematically in Fig. 4 as well as superimposed onto the PIV-derived turbulent kinetic energy (TKE) field in Fig. 5. The Pitot data were collected at discrete survey stations spanning from $x = 355.6$ mm (14 in) to $x = 584.2$ mm (23 in) at 12.7 mm (0.5 in) spacing. Additional surveys were made at half the spacing from $x = 469.9$ mm (18.5 in) to $x = 508.0$ mm (20 in) to better resolve the interaction region. Hot-wire measurements were applied only in this compact spatial region due to their time-intensive collection and processing. The PIV data spans a trapezoidal region with a wall-normal extent of $\overline{y} \leq 25$ mm from $x = 406.4$ mm to $x = 569.0$ mm (see Fig. 8 in Ref. 9). The normalized axial dimension, $(x - x_i)/\delta_1^*$, which will be used throughout the remainder of this paper is also shown on the top axis of Fig. 4 to show its mapping to physical dimensions. The value for incoming boundary layer momentum thickness, δ_1^*, is taken from the result derived from detailed Pitot surveys of 2.95 mm [8]. This normalization by a fixed value facilitates straightforward comparisons between the various data sources but can introduce small spatial offsets if the incoming boundary layer scale (i.e. δ^*) varies. This should not be the case between the various experimental datasets, but could occur when incorporating CFD solutions into the comparison. See Ref. 12 for detailed comparison of the boundary layer parameters from the companion CFD solutions with the experimental data.

While PIV data is generally considered to provide a continuous field of data, the vector spacing in this experiment was 0.25 mm. This resolution is surpassed by both the hot-wire surveys in the wall-normal direction where data were taken at spacing as small as 50 µm to capture the high-gradient region of the boundary layer. Additionally, the extreme viewing angles of the PIV cameras constrained the minimum wall-normal distance where valid vectors could be obtained. Thus, while PIV provides a more dense dataset in the streamwise direction, the two probe-based techniques yield more detailed information deep within the boundary layer.

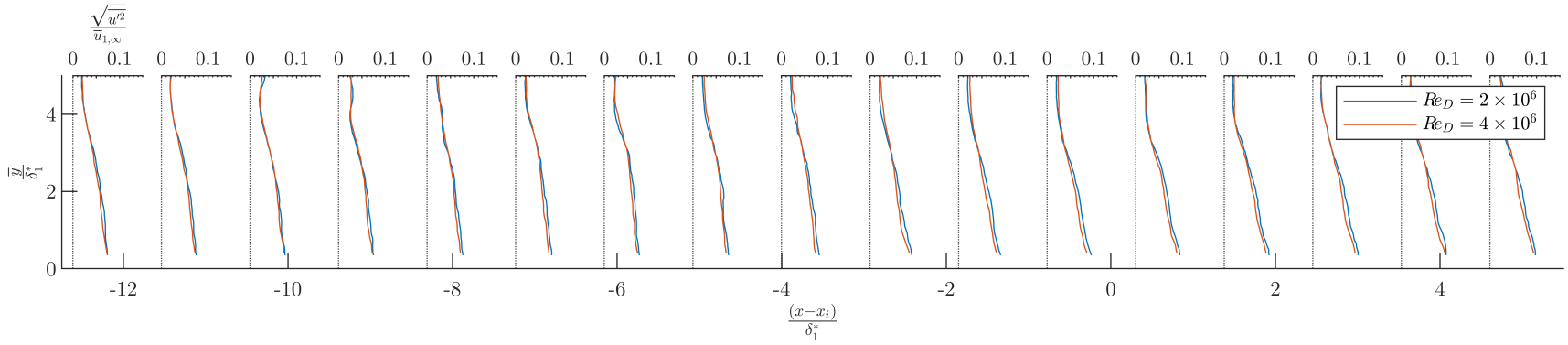


(a)

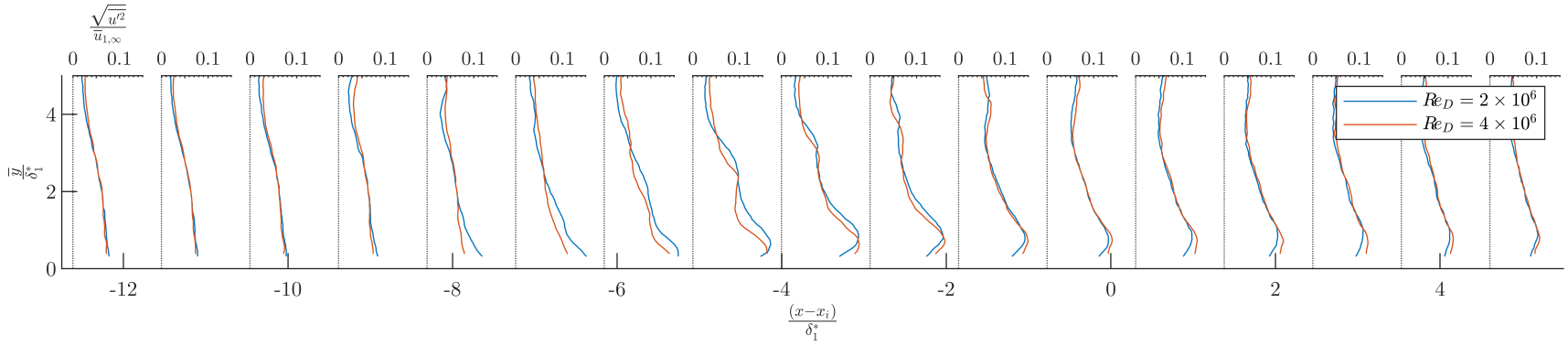


(b)

Fig. 2 Comparison of mean axial velocity profiles from PIV at bounding Reynolds number conditions in the (a) $\alpha = 10°$ and (b) $\alpha = 16°$ interactions.



(a)



(b)

Fig. 3 Comparison of r.m.s. axial velocity fluctuation profiles from PIV at bounding Reynolds number conditions in the (a) $\alpha = 10°$ and (b) $\alpha = 16°$ interactions.

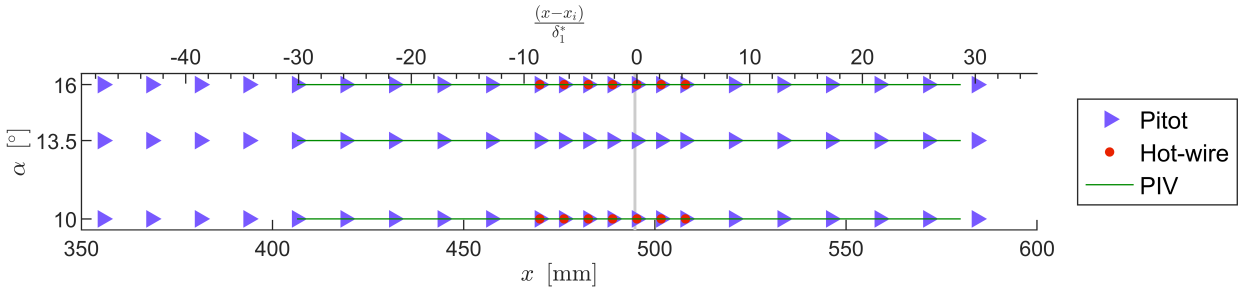


Fig. 4 Flowfield measurement stations. *Gray region indicates inviscid shock impingement region.*

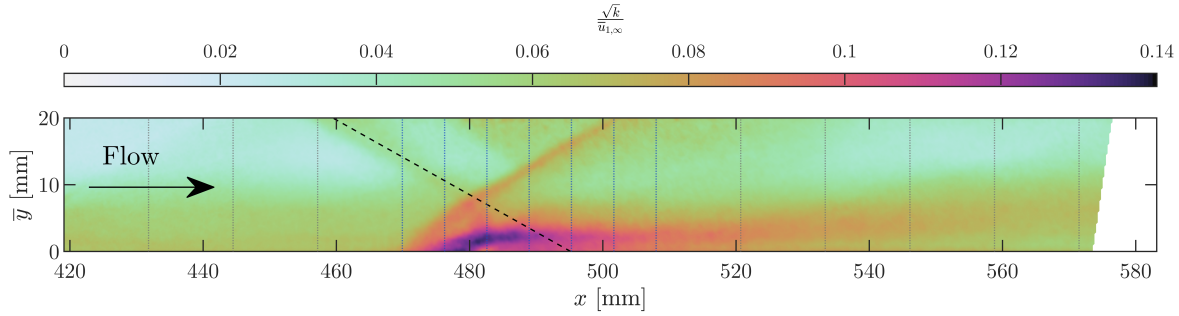


Fig. 5 Probe sampling stations overlaid onto PIV-derived TKE for the $\alpha = 16°$ case. *Blue vertical lines were sampled with both Pitot and hot-wire probes; stations indicated with gray were Pitot only.*

III. Results and Discussion

Flowfield variables being quantified by the various measurements include velocity, Pitot pressure, mass flux, and total temperature. Only in select regions can simplifying assumptions be made to allow for direct comparison between the data. Unfortunately, this does not include the region of the SWBLI where RANS models are likely to become inaccurate.

The governing equations for a turbulent compressible flowfield contain many additional cross- and triple-correlation terms which do not appear in their incompressible and laminar counterparts due to the fact that fluid density can vary not only spatially but also temporally. In turbulent flows the equations of motion can be expressed in a "Reynolds-averaged" form, which is typically defined as the decomposition of variables into their time-average and fluctuating components. This is shown for generic variable, a, as

$$a = \overline{a} + a' \tag{1}$$

$$\overline{a'} \equiv 0\,. \tag{2}$$

A density-weighted time-averaging method called "Favre-averaging" is defined as

$$\widetilde{a} \equiv \frac{\overline{\rho a}}{\overline{\rho}} \tag{3}$$

$$a'' \equiv a - \widetilde{a} \tag{4}$$

$$\tag{5}$$

where the Reynolds-averaged Favre fluctuation can be related to the density-velocity cross-correlation by

$$\overline{a''} = -\frac{\overline{\rho' a'}}{\overline{\rho}} = -\frac{\overline{\rho' a''}}{\overline{\rho}} \not\equiv 0 \tag{6}$$

(see Appendix for derivation). The Favre decomposition proves to be very convenient in expressing the conservation equations for compressible flows. In fact, the use of Favre-averaged variables proves necessary in RANS CFD to gather

the density-velocity correlation terms into the turbulent stresses in the averaged mass/momentum/energy equations. Conversion between Favre-averaged and Reynolds-averaged data is straightforward if the correlation between density and velocity is known, i.e.

$$\overline{u_i} = \widetilde{u_i}\left(1 - \frac{\overline{\rho' u_i'}}{\overline{\rho u_i}}\right). \tag{7}$$

In a idealized experimental dataset, both Reynolds- and Favre-averaged quantities would be known and linear turbulence closure solutions could be evaluated directly by comparing the eddy viscosity derived from true Reynolds stresses with the model value, i.e.

$$\mu_t = \frac{-\overline{\rho u_i'' u_j''} + \frac{2}{3}\overline{\rho} k \delta_{ij}}{2\hat{S}_{ij}} \tag{8}$$

where $k \equiv \frac{1}{2}\widetilde{u_k'' u_k''}$ and $\hat{S}_{ij}$ is the deviatoric (traceless) strain tensor, $\widetilde{S_{ij}} - \frac{1}{3}\frac{\partial \widetilde{u_k}}{\partial x_k}\delta_{ij}$. Unfortunately, the full complement of density, velocity (all 3 dimensions), and cross-correlations thereof are impossible to obtain concurrently. However, the mean strain, $\overline{S_{ij}} \equiv \frac{1}{2}\left(\frac{\partial \overline{u_i}}{\partial x_j} + \frac{\partial \overline{u_j}}{\partial x_i}\right)$, and Reynolds stress,

$$-\tau_{ij}^t \equiv \overline{\rho u_i'' u_j''} = \overline{\rho}\widetilde{u_i'' u_j''} = \overline{\rho}\overline{u_i' u_j'} + \overline{\rho}\overline{u_i''}\overline{u_j''} - \overline{u_i''}\,\overline{\rho' u_j'} - \overline{u_j''}\,\overline{\rho' u_i'} + \overline{\rho' u_i' u_j'}, \tag{9}$$

tensors contain several terms which are individually measurable, as will be discussed. An additional difficulty with applying this method to measured data is the appearance of deviatoric strain in the denominator. For the normal components, this value is nearly zero except in regions of strong acceleration and the derived eddy viscosity value is highly sensitive to errors in the turbulent normal stress values. Furthermore, if the turbulent viscosity does not carry an extremely large value, the normal components are nearly identical and the numerator is everywhere nearly zero. Thus, this analysis is limited in application to the primary shear component, $\overline{u'v'}$, only.

Pitot pressure measurements alone provide only the local time-averaged total pressure of the flowfield downstream of the probe-induced shock-wave in a supersonic flow. In regions of the flow where the local static pressure is known, the ratio of Pitot and static pressure can be used to compute the local Mach number of the undisturbed local flow assuming (1) the probe can be adequately aligned with local flow direction, (2) mild turbulence intensity, and (3) minimal velocity gradient across the scale of the probe face [13]. To convert Mach number data into velocity units for comparison with other measured data, local static temperature must be determined. This can be accomplished through synthesis with other measurements for by applying a temperature-velocity relation, such as the Crocco-Busemann/Walz equation [14] or Whitfield & High expressions [15]. The latter is preferred because it captures the overshoot in mean total temperature which is observed in adiabatic compressible boundary layer flows. The overshoot was found to closely match the total temperature measurements made with hot-wire probes in the upstream boundary layer of the current configuration [7, 8]. However, the error incurred by computing velocity from Pitot probe data using the Crocco-Busemann relation at this Mach number is negligible [7, 8]. If the local static pressure is unknown, which is the case for most of the flowfield in the current study, the Pitot pressure measurements cannot be reduced beyond a normalization by the freestream value, as presented in Refs. 7, 8.

PIV measures velocity directly (u, v, and w), which is the most typical flowfield variable to analyze when studying fluid motion which are dominated by inertial forces in the absence of strong compressibility. In many investigations, the PIV-derived kinematic stresses, $\overline{u_i' u_j'}$, are used as surrogates for the compressible Reynolds stresses, $\overline{\rho u_i'' u_j''}$, (see Eq. (9)) in the absence of information about the mean and fluctuating density fields which are required for Favre-averaged terms [16]. The PIV technique is constrained by the finite size of the interrogation windows which are applied for the image cross-correlation (limits velocity dynamic range), finite sensor pixel size (limits minimum resolvable velocity increment) and by the inertial behavior of the seed particles (limits ability to resolve high-frequency velocity fluctuations).

Hot-wire measurements are directly sensitive to heat transfer between the wire and surrounding gas. This information can be reduced to measurements of mean mass flux normal to the wire, $\rho \| \mathrm{proj}_{x-y} \vec{U} \|$, in flows without significant probe yawing (typically further assumed identical to $\overline{\rho U}$) and flow total temperature, $\overline{T_t}$, using the aerodynamic calibration procedure outlined in Ref. 7. Additionally, by acquiring data at various wire overheat ratios, the fluctuation intensity in mass flux ($\overline{(\rho U)'^2}$), total temperature ($\overline{T_t'^2}$), and their cross-correlation ($\overline{(\rho U)' T_t'}$) can also be determined [8, 17]. Because the technique is sensitive to mass flux instead of velocity, the data provided by this measurement is advantageous in compressible flows where "Favre-averaged" quantities are commonly used in the governing equations for RANS modeling. For example, with knowledge of the mean density field, as in the incoming boundary layer, the Favre-averaged velocity, $\widetilde{u}$, is readily computed.

The hot-wire data may be further reduced to Reynolds-averaged velocity measurements with the assumption that acoustic energy is small and the flow temperature fluctuations are isobaric: $\frac{\rho'}{\overline{\rho}} = -\frac{T'}{\overline{T}}$. This implies that the turbulence induces very little compressibility in the flow ($M_t < 0.3$) and the incompressible turbulent pattern is merely convected along by the compressible mean flow. The equations become [7, 17]

$$\overline{\rho u} = \bar{\rho}\bar{u} + \overline{\rho' u'} = \overline{\rho}\sqrt{\gamma R g_c \overline{T}_t}\frac{\overline{M}}{\sqrt{1+\frac{\gamma-1}{2}\overline{M}^2}} + \overline{\rho' u'} \tag{10}$$

$$\overline{\rho' u'} = \frac{\overline{\rho u}}{(\alpha+\beta)^2}\left[\alpha\beta\frac{\overline{(\rho u)'^2}}{\overline{(\rho u)}^2} - \frac{\overline{T_t'^2}}{\overline{T}_t^2} + (\beta-\alpha)\frac{\overline{(\rho u)' T_t'}}{\overline{\rho u}\,\overline{T}_t}\right] \tag{11}$$

$$\alpha \equiv \left(1+\frac{\gamma-1}{2}\overline{M}^2\right)^{-1} \tag{12}$$

$$\beta \equiv \alpha(\gamma-1)\overline{M}^2 \tag{13}$$

where measured values of $\overline{\rho u}$ and the 3 turbulent intensities, $\frac{\overline{(\rho u)'^2}}{\overline{(\rho u)}^2}$, $\frac{\overline{T_t'^2}}{\overline{T}_t^2}$, and $\frac{\overline{(\rho u)' T_t'}}{\overline{\rho u}\,\overline{T}_t}$, can be applied to solve for $\overline{M}$ and $\overline{\rho' u'}$ at each location in a survey.

This procedure was applied to the incoming boundary layer data in Ref. [7], where the static pressure profile normal to the wall was assumed to be constant at the wall value ($\rho = \frac{\overline{P_w}}{\gamma R \overline{T}}$). As with comparisons between the Pitot probe and PIV data, the simplifying assumptions that allow for the direct conversion of data between the measured quantities are invalid in the SWBLI region where static pressure is not constant. Instead, density information from another source must be leveraged to bridge between the various measured mean quantities.

Fluctuating components are further complicated by the correlation of thermodynamic variables with the velocity field. For example, the mass flux fluctuations which are quantified by the hot-wire measurements can be expanded as

$$(\rho u)' = (\overline{\rho} + \rho')(\overline{u} + u') - \overline{\rho u} \tag{14}$$

$$\frac{\overline{(\rho u)'^2}}{\overline{\rho}^2\overline{u}^2} = \frac{\overline{u'^2}}{\overline{u}^2} + \frac{\overline{\rho'^2}}{\overline{\rho}^2} + 2\frac{\overline{\rho' u'}}{\bar{\rho}\bar{u}} + 2\frac{\overline{\rho' u'^2}}{\bar{\rho}\bar{u}^2} + 2\frac{\overline{\rho'^2 u'}}{\bar{\rho}^2\bar{u}} \tag{15}$$

which illustrates the difficulty in directly comparing the turbulent quantities from the hot-wire and PIV datasets (as well as with the Favre-averaged fluctuations from RANS solutions). These relations may be simplified by applying assumptions about the relative order of magnitude of the terms, as will be discussed.

The mass flux observed by the hot-wire measurement is typically assumed to be aligned with the direction of freestream flow ($\|\vec{U}\| = U$). For the mean flow upstream of the interaction where the flow not turned significantly, this is a good assumption since $\left|\frac{\overline{v}}{\overline{u}}\right| < 0.02$ and $\overline{w} = 0$. Within the interactions studied herein, the deviation of the mean velocity vector from axial does not exceed $-9.5°$ to $+7.5°$ in the PIV data and, thus, the overstatement of axial mass flux due to flow angularity is on the order of at most 1.4% (see Appendix).

The effect of three-dimensional turbulent fluctuations is more nuanced. Significant levels of fluctuation in v and w implies that the heat transfer process which drives the hot-wire measurements may not be solely driven by the axial component of velocity fluctuations, as is typically assumed in boundary layer studies. If the turbulent intensity in the direction of the wire axis is weak enough to be considered incompressible, the typical "cosine-law" dependence [18] applied to incompressible flow measurements may be applied. This implies that the wire is only sensitive to the projection of $\rho\vec{U}$ onto the wire-normal plane. This is in contrast to the analysis applied to inclined-wire measurements in compressible flow where significant yawing velocity induces a coupling of the probe response and local Mach number [19].

For the current dataset, the consequence of considering non-negligible v' and w' for a probe which is not perfectly aligned to the local streamline is that data typically attributed as axial mass flux fluctuations, $(\rho u)'$, also contain a dependence to fluctuations in the wire binormal direction (normal to both the local flow vector and the wire axis). In the case where the probe is equally sensitive to mass flux fluctuations within the plane normal to wire (x-y plane here), the quantity being measured is (see Appendix)

$$\frac{\overline{E'^2}}{S_{\rho U}^2} = \overline{(\rho u)'^2}\left[1 + 2\frac{\overline{\rho v}}{\overline{\rho u}}\frac{\overline{(\rho u)'(\rho v)'}}{\overline{(\rho u)'^2}} + \left(\frac{\overline{\rho v}}{\overline{\rho u}}\right)^2\frac{\overline{(\rho v)'^2}}{\overline{(\rho u)'^2}}\right] \tag{16}$$

which closely resembles the intended quantity $\overline{(\rho u)'^2}$ when the flow angularity and wall-normal turbulence level are low.

While information on the intensity of density fluctuations is not available, the PIV data can provide an order-of-magnitude estimate of the error induced in the hot-wire measurement by misalignment of local streamlines from axial by evaluating two cases: negligible density fluctuations or in the assumption that pressure fluctuations are small and, thus, the density fluctuation intensity follows directly with axial velocity (Strong Reynolds Analogy, discussed in detail later). These are shown for the $\alpha = 16°$ case, which contains the strongest flow turning, in Fig. 6. Here, the effect is negligible in the incoming boundary layer, as expected, and the overstatement of axial turbulence does not exceed 4% in the interaction region. This is due to a combination of small flow angularity and dominance of the axial turbulence in regions where flow angularity is present.

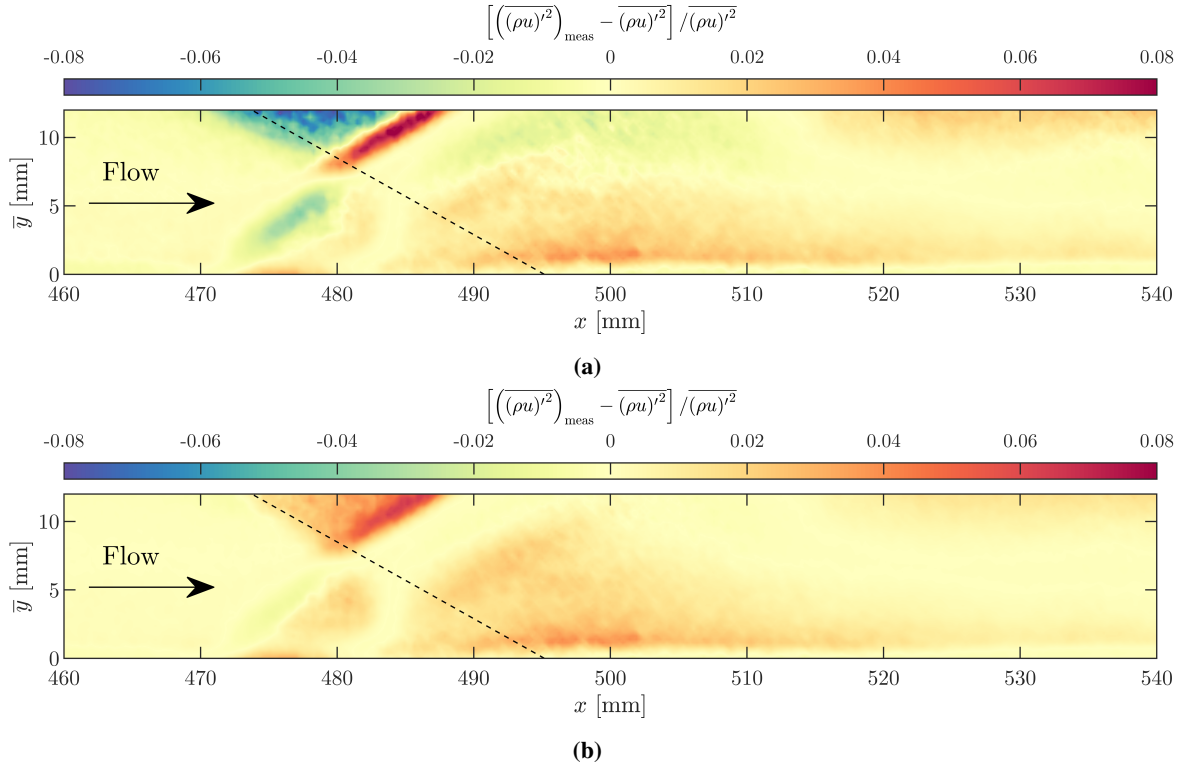


Fig. 6 Estimate of flow angularity effect on axial mass flux turbulence levels derived from single-normal hot-wire probes based on PIV data from the $\alpha = 16°$ interaction under the assumption of (a) negligible density fluctuations or (b) perfect ρ-u correlation.

Conversely, the length of the sensing element (wire) can bias the measurement of turbulent intensity toward lower values [20–22]. A wire which is long relative to the spatial scale of the turbulence incurs a spatial-averaging effect while a wire with a low length-to-diameter ratio can be biased by heat conduction to the support prongs. Either of these scenarios result in attenuation of the observed turbulent intensity. The combination of these requirements drives the wire to the minimum practical wire diameter in high Reynolds number flow, which is constrained by wire fragility at supersonic speeds.

A. Flowfield Thermodynamic Property Estimation

The primary source for thermodynamic properties of the flowfield used to bridge between the various measured quantities is CFD simulations. While implicit large-eddy simulations have been applied at reduced Reynolds number [23], RANS solutions at conditions matched to the experiment [12] are utilized herein to ensure consistency of the spatial scales. While solutions from various solvers and turbulence models are available, only a select set was applied here to supplement the experimental data. Specifically, solutions from NASA's FUN3D and VULCAN-CFD solvers utilizing two common turbulence models: the Spalart-Allmaras (SA) model and a version of the Menter Shear Stress Transport $k - \Omega$ model which utilizes a vorticity-based production equation (SST-V). For further detail on the relative

accuracy of the various solution methods, see Ref. 12. The reader is cautioned that the CFD solutions are not taken as "ground-truth" in the comparisons herein, but instead included as an independent additional data source. The intrinsic limitations of the RANS turbulence models and consequent inaccuracy in computed flowfield is acknowledged.

The time-averaged thermodynamic property fields may be derived from PIV measurement in a 2D flowfield by the procedure outlined by Van Oudheusden [24] which will be referred to here as "pressure-from-PIV". By invoking the Euler momentum equation, an assumption of adiabaticity and negligible density fluctuations, the local pressure gradient can be computed directly from velocity data. The equations, in conservative form as suggested therein, are

$$\begin{gathered}
\nabla p = -\nabla\left(\rho\vec{U}\otimes\vec{U}\right) \\
\left(\delta_{ij}R\overline{T}+\overline{u_iu_j}\right)\frac{\partial\ln(\overline{p}/p_\infty)}{\partial x_i} = -\left(\frac{\partial\overline{u_iu_j}}{\partial x_i}-\frac{\overline{u_iu_j}}{\overline{T}}\frac{\partial\overline{T}}{\partial x_i}\right) \\
\begin{bmatrix} RT+\overline{uu} & \overline{uv} \\ \overline{uv} & RT+\overline{vv} \end{bmatrix}\begin{bmatrix} \frac{\partial\ln(\overline{p}/p_\infty)}{\partial x} \\ \frac{\partial\ln(\overline{p}/p_\infty)}{\partial y} \end{bmatrix} = \begin{bmatrix} -\left(\frac{\partial\overline{uu}}{\partial x}+\frac{\partial\overline{uv}}{\partial y}-\frac{\overline{uu}}{\overline{T}}\frac{\partial\overline{T}}{\partial x}-\frac{\overline{uv}}{\overline{T}}\frac{\partial\overline{T}}{\partial y}\right) \\ -\left(\frac{\partial\overline{uv}}{\partial x}+\frac{\partial\overline{vv}}{\partial y}-\frac{\overline{uv}}{\overline{T}}\frac{\partial\overline{T}}{\partial x}-\frac{\overline{vv}}{\overline{T}}\frac{\partial\overline{T}}{\partial y}\right) \end{bmatrix}
\end{gathered} \tag{17}$$

where temperature is computed using a slightly modified equation, which includes the recovery factor, r, to account for non-unity Prandtl number:

$$\frac{\overline{T}}{T_\infty} = 1 + r\frac{\gamma-1}{2}\overline{M}_\infty^2\left(1-\frac{\overline{u}_i\overline{u}_i}{\overline{\|\vec{U}\|}_\infty^2}\right) \tag{18}$$

The implicit assumption required for application of Eq. (17) in a flowfield which is significantly affected by viscous forces, such as the current SWBLI, is that the pressure gradient terms which must be integrated are negligibly influenced by viscous stresses. This was demonstrated in Ref. 24 for both transonic airfoil and planar impinging SWBLI data and will be assessed for the current dataset as well.

An example derived temperature field from the current dataset and the corresponding Mach number values are shown in Fig. 7. This information can then be used to solve the 2×2 system shown in Eq. (17) at each spatial location to compute the 2D gradient of the logarithm of pressure. This is shown for the same example case in Fig. 8 where the data has been smoothed by a 3×3 median filter to mitigate noise.

In order to compute the pressure field, the gradient data must be spatially integrated. In Ref. 24, this was accomplished with a spatial marching technique from an initialized region of known pressure. In the current dataset, a convenient region to use is the incoming freestream flow. A simple spatial marching technique was applied to spatially integrate the gradient into pressure fields as shown in Fig. 9. This method was selected for its simplicity, applicability to the current flowfield where the solution can be marched from the undisturbed incoming freestream flow, and previous success in a similar flowfield [24]. Solutions based on the Poisson equation, while more mathematically rigorous, would require boundary conditions to be specified on the entire periphery, which is not known precisely a priori in the current flow. For example, prescribing the behavior of the pressure field at the upper boundary presents a challenge downstream of the incident shock wave which is followed by a region of continuous compression, then expansion from the centerbody shoulder, and finally the reflected shock whose precise position depends on the viscous SWBLI behavior. The numerical scheme applied here utilized second order accurate methods for the spatial derivatives and a trapezoidal method to integrate the pressure gradient derived from the average of the available neighbors. To assess the accuracy of this method, the derived parameters can be compared directly with CFD solutions and probe measurement data.

The contribution of the turbulent terms was shown to be negligible in prior SWBLI application [24]. While it is trivial to include the fluctuating terms when performing the calculation, the increased relative uncertainty in higher moments of the velocity distribution (and spatial derivatives thereof) in a general dataset makes their omission advantageous. The relative difference in resulting parameters derived by including or omitting the turbulent terms was evaluated for the current dataset, where the large number of velocity field samples should well-resolve the turbulent intensities. In particular, the case in the current dataset which contains the strongest turbulence, $\alpha = 16^\circ$ was selected for evaluation. The results are plotted in Fig. 10. The three terms plotted are all related to one another and, thus, show similar trend of the inclusion of turbulent terms driving a decreased value near the shock crossing and separation point and a near-wall increase in the recovering boundary layer. The reason for presenting all three parameters is to illustrate the magnitude of the change in parameter value. While the static pressure is locally altered by up to 10% of the freestream pressure, the two parameters which will be used to compare with other measurements, density and Pitot pressure, are less affected by the inclusion of the fluctuation terms. This is driven by the fact that the largest changes in

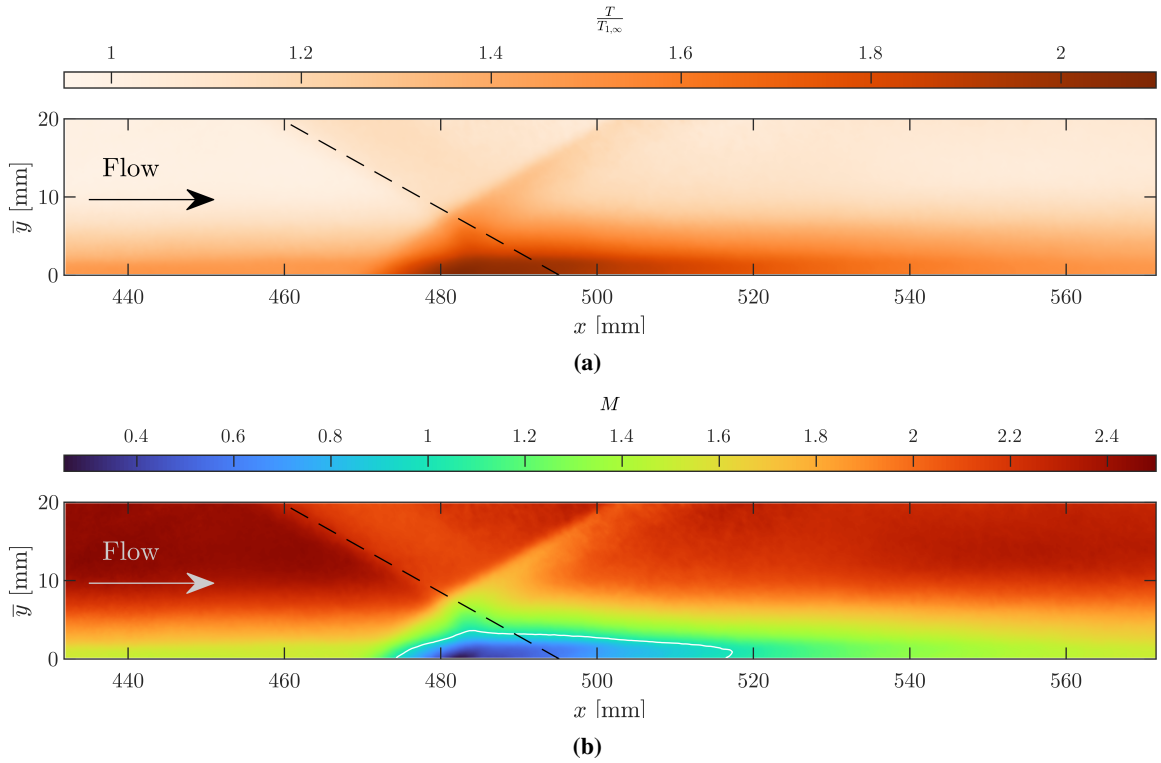


Fig. 7 PIV-derived thermal properties for the $\alpha = 16°$ interaction at $Re_D = 4 \times 10^6$: (a) temperature and (??) Mach number (white contour highlights sonic line).

pressure occur in regions of reduced Mach number, which attenuates the extremes observed in the other two variables. Thus, both derived thermodynamic fields (computed with and without inclusion of the fluctuation terms) will be carried forward through the analysis in this paper to gauge the relative accuracy of each.

The pressure-from-PIV result can be further evaluated by comparing the near-wall flowfield pressure with that measured directly with wall taps in the conventional test section. Figure 11 shows this for both the $\alpha = 10°$ and $\alpha = 16°$ cases. Considering the typical difficulty in deriving quantitative wall measurements from flowfield data, the pressure inferred from the PIV velocity field follows the trends of the measured wall pressure quite well in both while somewhat over-predicting the peaks in the profile. The discrepancy in pressure ratio is not unexpected considering the difficulty in obtaining accurate PIV in that region with downward-looking cameras.

The congruence in the shape of these pressure profiles further strengthens the previous assertion that the pressure-from-PIV method is able to broadly capture the behavior of this flowfield. Perhaps the most consequential result from this comparison is the agreement in the location of the initial pressure rise which indicates the mean location of upstream influence from the reflected shock foot. This indicates congruence between the measurements on the overall scale of the interaction and in the registration of the measurement spatial locations. This is quite important for CFD validation efforts which seek to make comparison in solution variables both within the flowfield (measurements require a finite offset from the wall) and on the domain boundary.

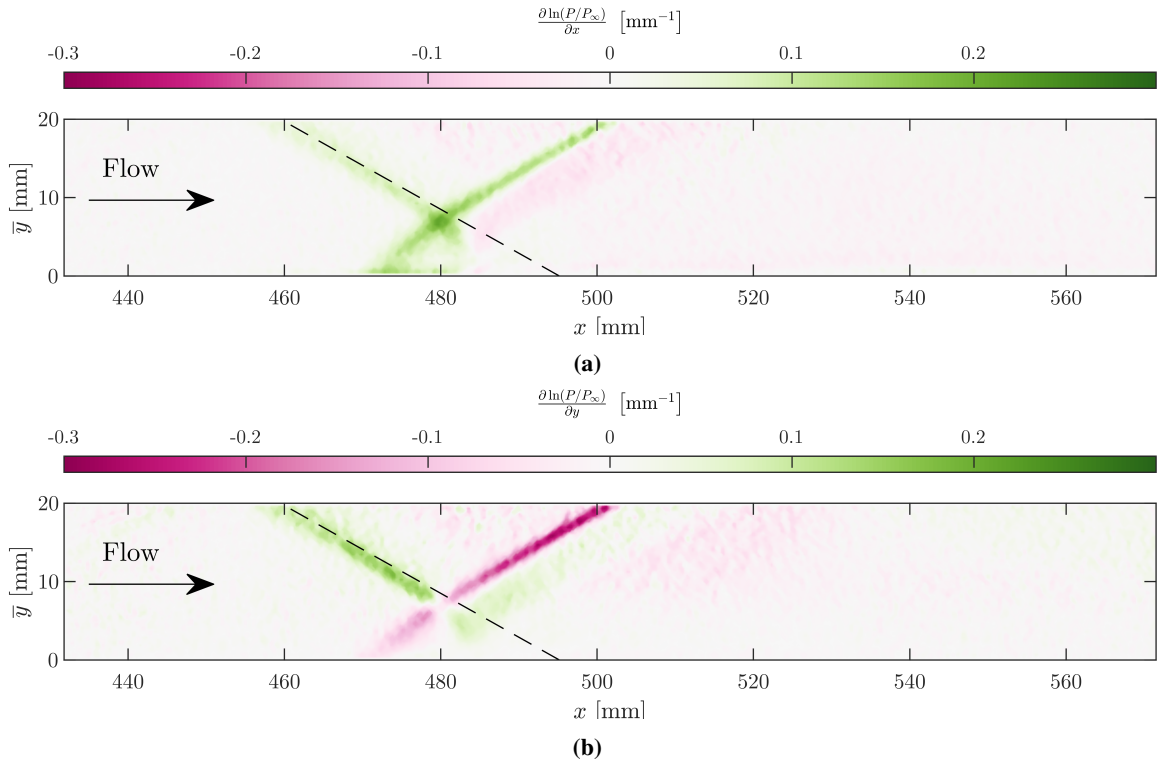


Fig. 8 PIV-derived pressure gradient for the $\alpha = 16°$ interaction at $Re_D = 4 \times 10^6$: (a) axial component, (b) wall-normal component.

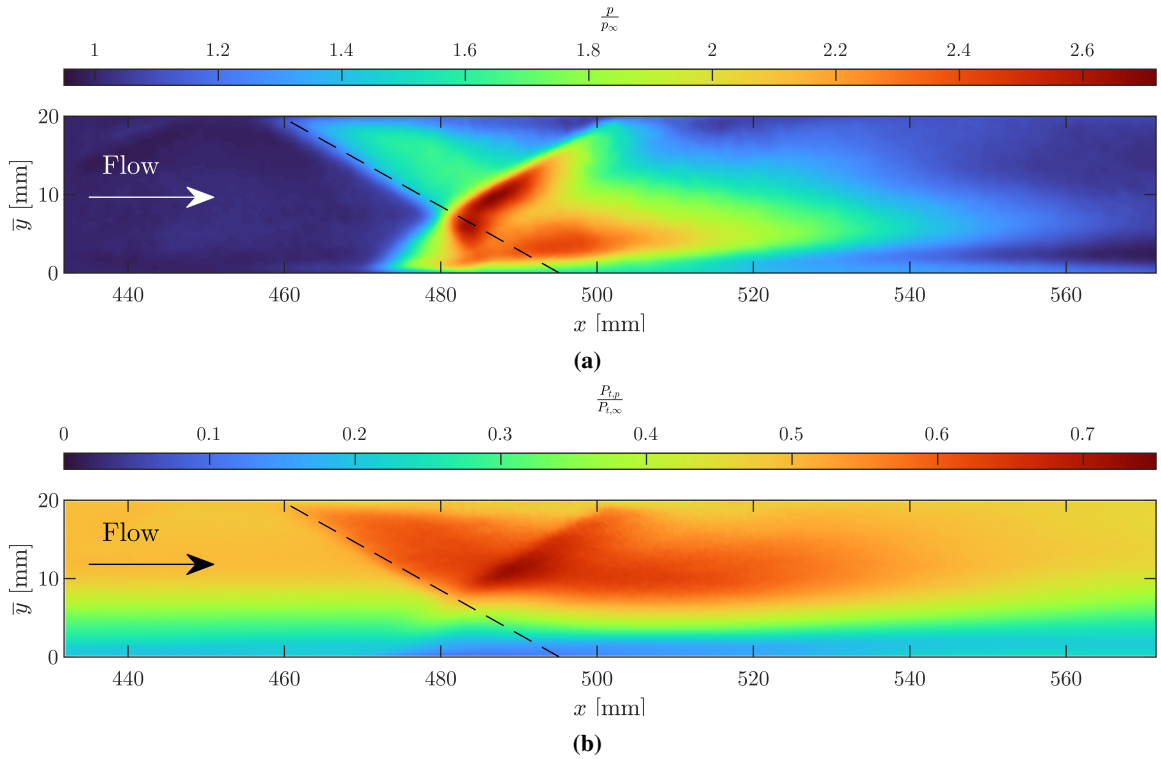


Fig. 9 PIV-derived pressure fields for the $\alpha = 16°$ interaction at $Re_D = 4 \times 10^6$: (a) static , and (b) Pitot pressure.

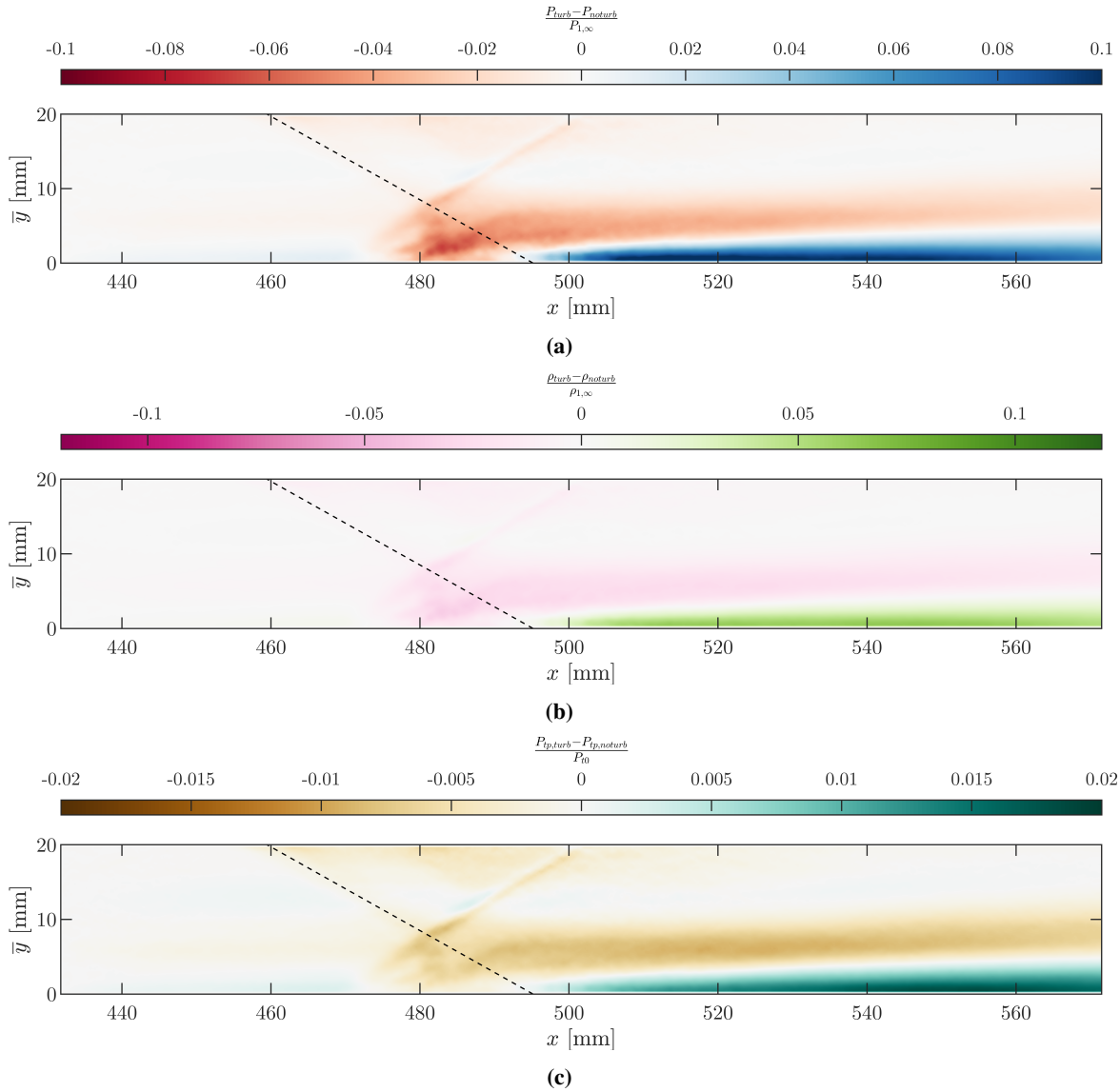
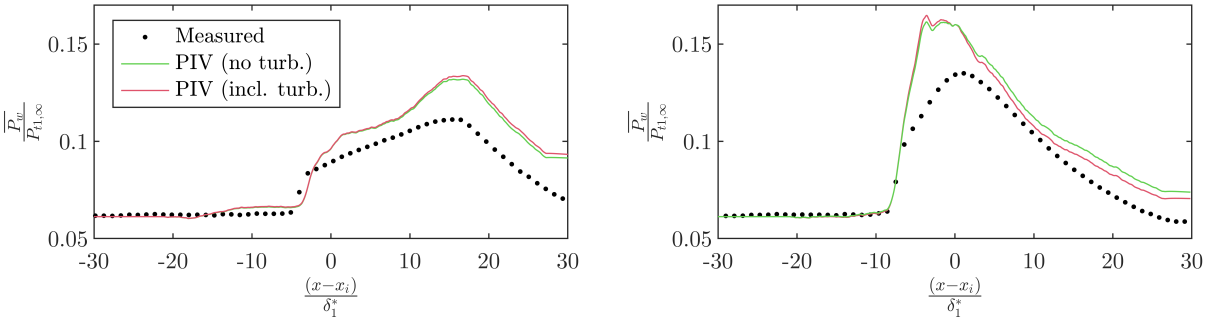


Fig. 10 Difference in flowfield parameters derived from PIV in the $\alpha = 16°$ interaction when including/neglecting turbulent terms in the calculation: (a) static pressure, (b) density, (c) Pitot pressure.



(a) $\alpha = 10°$ **(b)** $\alpha = 16°$

Fig. 11 Surrogate wall pressure traces derived from PIV in comparison with measurements.

B. Comparison of Measured Quantities

1. Incoming Boundary Layer

As discussed in the previous section, the assumption of constant static pressure in the wall-normal direction allows for direct measurement-to-measurement comparisons to be made in the incoming turbulent boundary layer. The comparisons made between PIV and probe measurements shown in Ref. 9 will be expanded upon here. In particular, the assumptions related to various forms of the Strong Reynolds Analogy (SRA) [25] will be evaluated. Additionally, CFD data will provide reference checks on the derived quantities (density, etc.).

The boundary layer velocity profile as measured by all 3 techniques is compared in detail in this section. Figure 12 shows a comparison between the PIV and Pitot-derived velocity data, as shown in Ref. 9. Overall, the data from disparate measurements agree well, although the PIV data shows a distinctly higher velocity at the boundary layer edge than Pitot profiles at either azimuthal position.

Comparisons to hot-wire measurements were not made therein due to the difference in definition of upstream boundary layer sampling station. The station defined in Ref. 7 as the upstream boundary (showing excellent agreement between Pitot and hot-wire probes) was $x = 355.6\,\text{mm}$ (14 in) is further upstream than PIV data could be obtained. However, Pitot surveys were performed at regular spacing such that one of the further downstream stations (but still well upstream of shock impingement) could be utilized for comparison with PIV. With some normalization of the data to account for boundary layer growth, the data at disparate stations should still be able to be compared directly under the assumption that streamwise pressure gradient effects are minimal.

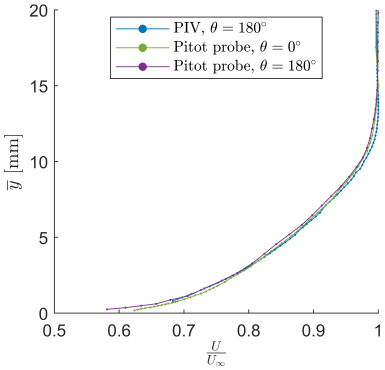


Fig. 12 Mean axial velocity profiles in the incoming boundary layer at $x = 419.1\,\text{mm}$ (16.5 in) and $Re_D = 2\times10^6$.

For the mean velocity field, the Strong Reynolds Analogy [25] implies that

$$\frac{\widetilde{u}-\overline{u}}{\overline{u}} = R_{\rho' u'}(\gamma-1)M_t^2 \tag{19}$$

where $R_{\rho' u'}$ is the density-velocity correlation coefficient defined as

$$R_{\rho' u'} \equiv \frac{\overline{\rho' u'}}{\sqrt{\overline{\rho'^2}}\sqrt{\overline{u'^2}}} = \frac{\frac{\overline{\rho' u'}}{\overline{\rho}\overline{u}}}{\sqrt{\frac{\overline{\rho'^2}}{\overline{\rho}^2}}\sqrt{\frac{\overline{u'^2}}{\overline{u}^2}}}\,. \tag{20}$$

Equation (19) yields differences between Favre- and Reynolds-averaged velocity of $< 1.5\%$ for the observed value for $R_{\rho' u'} = 0.8$ and turbulence Mach number, $M_t \equiv \frac{\sqrt{\overline{u'^2}}}{\overline{a}}$, of 0.2 [26]. Estimates using the current PIV data and an assumption of uniform total temperature in the incoming boundary layer are in agreement with this level of turbulence Mach number and resulting difference between Favre- and Reynolds-averaged values.

This section will present turbulence quantities from hot-wire (velocity, density, and their correlation) and PIV measurements (velocity only). Figure 13 shows the velocity turbulence level measured in the undisturbed incoming boundary layer. The relatively high level of turbulence observed outside the boundary layer in the PIV data is indicative of the noise floor of that measurement exceeding the true turbulence intensity. This is evident when considering the

superior dynamic range of the hot-wire probe and its assessment of the freestream turbulence level to be 0.3% of the mean velocity. The noise floor of the PIV measurement apparatus is set by a combination of factors contributing to the random error, the foremost of which being the stereoscopic reconstruction error and accuracy of the peak detection relative to the finite resolution of the sensor. As discussed in Ref. 9, the average disparity resulting from the stereoscopic reconstruction in the freestream for this dataset is 0.25 pix, which amounts to an error of 1.5% of $\overline{u}_\infty$. Similarly, the typical correlation peak error of 0.1 pix will add an additional 0.5% to the error which amounts to the noise floor observed in Fig. 13.

The PIV measurements can be corrected if the noise is assumed to be uncorrelated to the turbulent fluctuations by subtracting the variance observed in the incoming freestream from the mean squared deviation at every point as

$$\sqrt{\overline{u_i'^2}} = \left(\overline{u_{i,meas}'^2} - \overline{\sigma_{u_i,\infty}^2}\right)^{1/2} . \tag{21}$$

After applying this correction, the turbulence intensity from the two measurement techniques is in better agreement. The PIV profile still exhibits turbulence levels in the outer portion of the layer which match that of the hot-wire measurements. As the wall is approached, the PIV-derived turbulence levels begin to fall below the hot-wire values. For the near-wall region, the PIV data approach the empirical wall-wake law of Smits [27] when using the high Reynolds number constants proposed therein and applying the appropriate compressible flow transformations. The hot-wire data exhibits elevated turbulence much deeper into the layer, only approaching the empirical result at the last point in the profile. Both measurements suggest that the turbulence level over most of the boundary layer is elevated from typical flat plate boundary layer levels by up to 3.5% of the local mean velocity. The persistence of turbulence near the boundary layer edge beyond the empirical relation is consistent with other experimental and DNS datasets used to fit the model; thus, the discrepancy in Fig. 13 at $\frac{y}{\delta_{99}} > 1$ is due to a shortcoming of the simple analytical description.

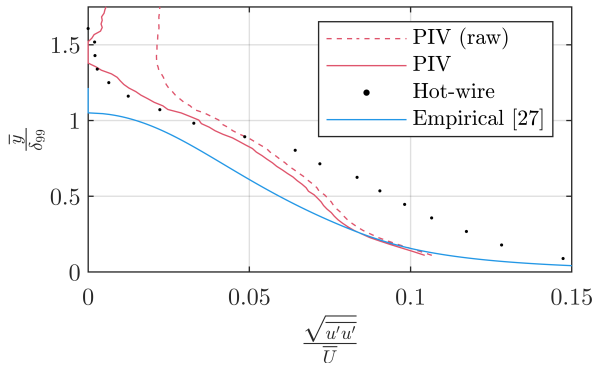


Fig. 13 Axial velocity turbulence intensity in the incoming boundary layer.

The SRA can also be utilized to convert between velocity and mass flux fluctuation data. If the higher-order terms in Eq. (15) are neglected, the normalized mass flux fluctuation level is

$$\frac{\overline{(\rho u)'^2}}{\overline{\rho}^2\overline{u}^2} = \frac{\overline{u'^2}}{\overline{u}^2} + \frac{\overline{\rho'^2}}{\overline{\rho}^2} + 2\frac{\overline{\rho' u'}}{\overline{\rho}\,\overline{u}} = \frac{\overline{u'^2}}{\overline{u}^2}\left[1 + 2R_{\rho' u'}(\gamma-1)\overline{M}^2 + (\gamma-1)^2\overline{M}^4\right] \tag{22}$$

if we assume that the relation

$$\frac{\sqrt{\overline{\rho'^2}}/\overline{\rho}}{\sqrt{\overline{u'^2}}/\overline{u}} = (\gamma-1)\overline{M}^2 \tag{23}$$

derived for adiabatic, compressible turbulent boundary layers holds. While some aspects of the SRA (i.e. $\overline{T_t'^2} = 0$ and $R_{\rho' u'} = 1$) have been proven invalid [28, 29], Eq. (23) has been shown to derive its accuracy from the fact that $\overline{T'^2} \gg \overline{T_t'^2} - 2\overline{T_t' T'}$ which has been confirmed by direct numerical simulation in a Mach 2.5 turbulent boundary layer [30] as well as at more extreme conditions [31].

This can be converted to the freestream-normalized r.m.s value typically presented as

$$\frac{\sqrt{\overline{(\rho u)'^2}}}{(\overline{\rho u})_{1,\infty}} = \frac{\bar{\rho}\bar{u}}{(\overline{\rho u})_{1,\infty}} \frac{\sqrt{\overline{(\rho u)'^2}}}{\bar{\rho}\bar{u}} = \frac{\bar{\rho}}{\bar{\rho}_{1,\infty}} \frac{\sqrt{\overline{u'^2}}}{\bar{u}_{1,\infty}} \left[1 + 2R_{\rho' u'}(\gamma - 1)\overline{M}^2 + (\gamma - 1)^2 \overline{M}^4\right]^{1/2} \tag{24}$$

where the negligible turbulence level in the freestream allows $\bar{\rho}_\infty \bar{u}_\infty \approx \overline{\rho u}_\infty$ to be substituted in order to separate mass flux into its density and velocity components.

The density-velocity correlation has been extensively studied in compressible wall-bounded turbulence to develop models which accurately portray the coupling between momentum and energy transport [25, 28, 29, 31]. We can make our own assessment of this correlation using the hot-wire data by applying Eqs. (10) to (13), using Eqs. 17-18 in Ref. 17 to compute the fluctuation intensities in density and velocity. Figure 14 shows the result from the current dataset where the correlation is significant, as expected, with a slow decrease toward the wall. The value approaches other experimental [32] and computational [30, 33] measures in this Mach number regime which show values in the range 0.5 to 0.65, although the trend in the wall-normal direction is not confirmed therein. Interestingly, the agreement of this experiment with the lower values typically observed in computations diverges from the literature where compressible boundary layer experiments typically obtain values closer to 1. This phenomenon has previously been attributed to more intense total temperature fluctuations in the experiments, typically by a factor of 2 [30]. The current dataset may not be influenced to the same degree as previous experimental results using similar methods due to the large number of overheat ratios utilized. Figure 14 in Ref. 8 illustrates that the peak in the measured total temperature fluctuation profile decreases by nearly 50% when utilizing the full complement of 11 overheat ratios instead of just 3.

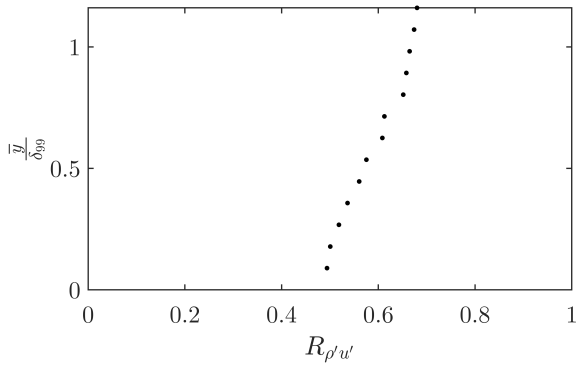


Fig. 14 Density-velocity correlation in the incoming boundary layer.

2. Interaction Region

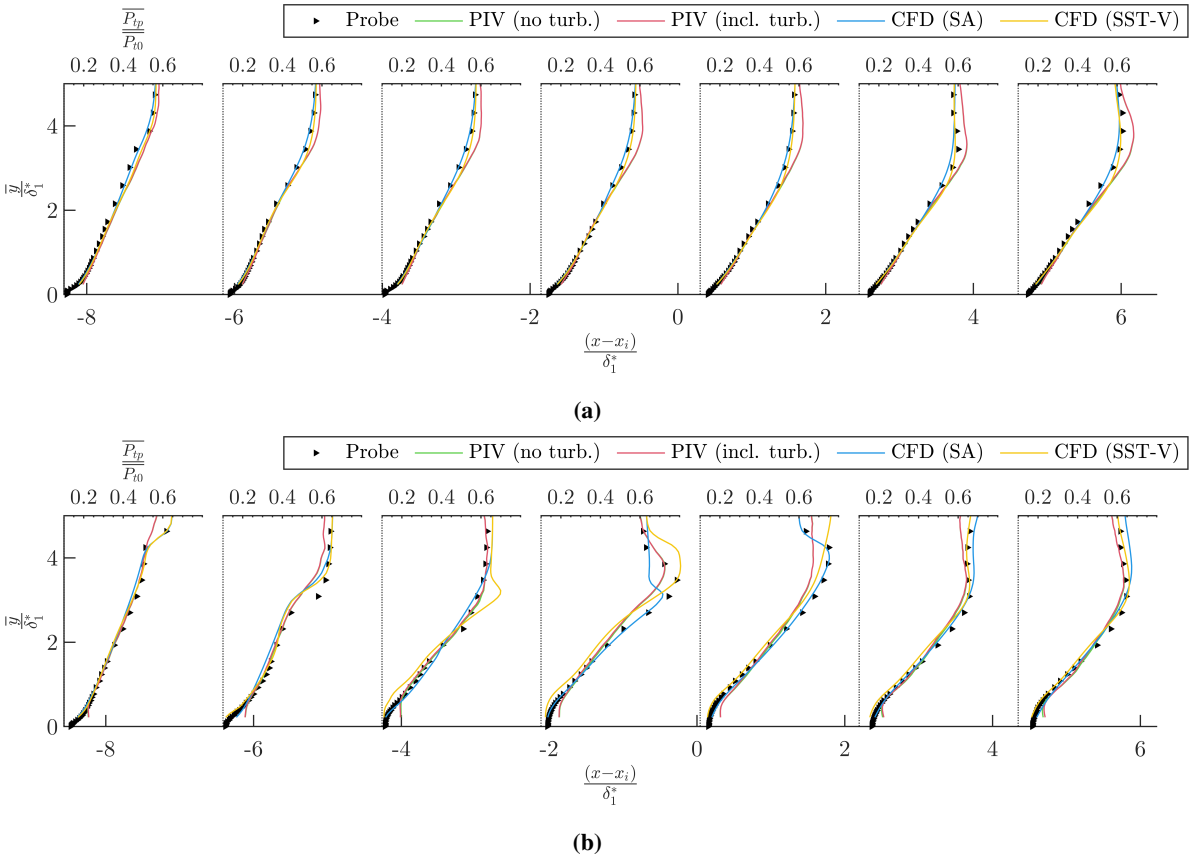
The region of the flowfield studied in this section is arbitrarily defined as the axial extent for which there is hot-wire data ($-0.29 \leq (x - x_i)/R \leq 0.16$) to emphasize the region around the initial pressure rise. At the upstream end of this region, the boundary layer shows very little influence of the SWBLI in the $Re_D = 4 \times 10^6$ case and behaves as if in equilibrium except for a jump observed outside the boundary layer which corresponds to the inviscid Rankine-Hugoniot relations. Closer to the impingement point, the influence of the reflected shock foot forward of the inviscid impingement point will be observable in both the mean quantities and turbulence measures. These will be coupled by the intermittency of the shock foot location.

In this region, the mean pressure field is not directly quantifiable by the measurement techniques applied, so the density field cannot be inferred even with an assumption of velocity-temperature relationship. This precludes the direct comparison of hot-wire and PIV data. However, pressure-from-PIV methods and companion CFD calculations provide the requisite information to bridge between the disparate measured quantities.

Data obtained by the pressure-from-PIV method described in Section III.A and through CFD simulation are compared with the Pitot probe measurements. These derived Pitot pressures are extracted along radial lines identical to the Pitot probe surveys to provide co-located data. Figure 15 presents the disparate datasets on a common set of axes for each probe station. Here, the dotted vertical lines denote the physical station on the lower abscissa while the scale for the data is given on the upper. The wall-normal coordinate is normalized by the incoming boundary layer displacement

thickness determined from the Pitot surveys to be 2.95 mm [8]. For the $\alpha = 10°$ case, the Pitot pressures derived from PIV data exhibit the same qualitative behavior as the probe measurements while exhibiting slightly higher values throughout the profile. This is most prevalent at the boundary layer edge and increases with downstream distance which is likely an artifact of the spatial marching integration scheme for the pressure field. Agreement is considerably better in the $\alpha = 16°$ interaction, where the PIV-derived result trends very close to the probe data. The largest discrepancy occurs approximately at the crossing point of the impinging and reflected shocks, which is where transient shock motions certainly muddy the interpretation of time-averaged measurements. Overall, the level of agreement is quite favorable considering the assumptions invoked in the pressure-from-PIV method.

For both cases, the CFD solutions presented were generated using the FUN3D solver. These solutions follow the probe data quite closely in both cases with some minor exceptions. In particular, the SST-V solution exhibits a small "hump" in Pitot pressure near the shock crossing point which is likely an artifact of slight spatial differences between the experiments and CFD which can be overemphasized in a discrete profile like those shown. Otherwise, this model appears to provide superior overall agreement with the measured data.



(a)

(b)

Fig. 15 Pitot pressure measurements in the interaction region for the (a) $\alpha = 10°$ and (b) $\alpha = 16°$ cases.

In Fig. 15, the difference between pressure profiles derived from PIV and the probe data are nearly imperceptible. In the weaker interaction, this is a result of the relatively low turbulence level generated. However, in the stronger interaction, the turbulence levels can become significant relative to the freestream values. As shown in Fig. 10, the Pitot pressure is altered by less than 2% of the freestream total pressure and the largest magnitudes occur in the recovery region which is not plotted here.

Similarly, Fig. 16a shows a direct comparison of the velocity and mass flux data from PIV and hot-wire measurement, respectively, at the more tightly-spaced stations of hot-wire measurement for the $\alpha = 10°$ interaction. It is clear that direct comparison of the measured quantities does not yield meaningful assessment of the agreement of the data. However, utilizing solutions obtained in the coordinating simulation study [12], the mean density field can be leveraged to eliminate the effect of the spatially-varying mean density. In particular, the solutions obtained with the FUN3D solver

package using both turbulence models are shown here. The results are shown in Fig. 16b, where the two measurement sets align quite well when using either CFD dataset. This agreement supports three interlinked findings:

1) the measured data from the hot-wire and PIV techniques are in congruence,
2) the CFD accurately captures the mean density behavior of this weak interaction, and
3) the role of density-velocity correlation is minor, as it is not accounted for here.

Freestream-normalized values can be expressed as

$$\frac{\overline{\rho}}{\overline{\rho}_{1,\infty}}\frac{\overline{u}}{\overline{u}_{1,\infty}} = \frac{\overline{\rho u} - \overline{\rho' u'}}{(\overline{\rho u})_{1,\infty}} \tag{25}$$

where the relative magnitude of $\overline{\rho' u'}$ is necessarily small relative to the mean mass flux to facilitate the agreement seen in Fig. 16b. This aligns with the fact that the boundary layer is only weakly perturbed in this case and follows from the scaling arguments made on the incoming boundary layer behavior regarding the influence of density-velocity correlation in low-supersonic Mach number flow.

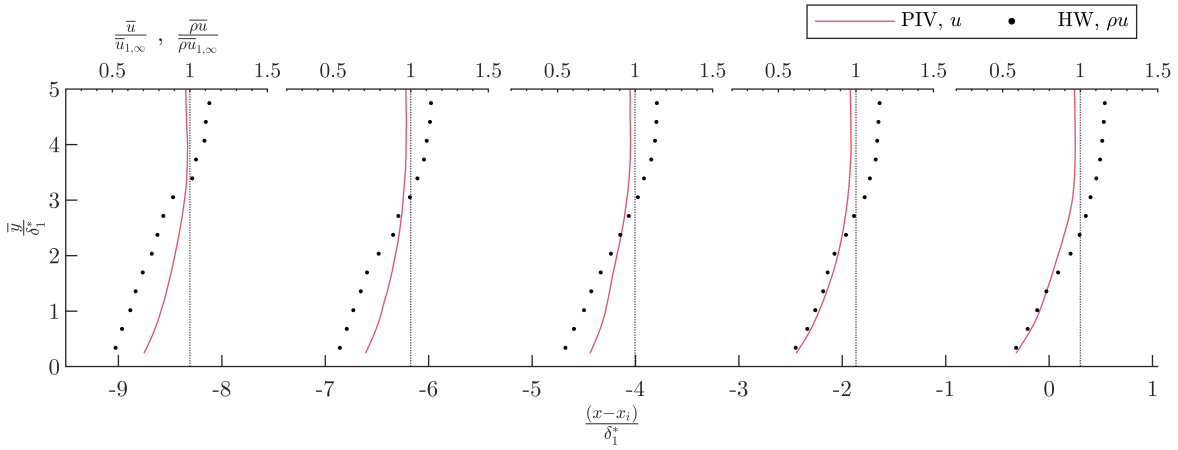
Both turbulence models shown here seem to accurately predict the flowfield in this unseparated case. This is unsurprising since these models are known to show most difficulty with portraying the flow separation which is only present in stronger interactions. This case instead serves as a baseline proof that the method of using density data from an external source to bridge between the PIV and hot-wire measurements is sound. For more thorough evaluation of the various models and solvers against this dataset, see Ref. 12.

For the $\alpha = 16°$ interaction, the increased pressure gradient leads to local separation behind the reflected shock foot and the generation of a region of high local turbulence in the shear layer above the separation zone. Profiles of mean mass flux are plotted in Fig. 17 in a fashion similar to the weaker interaction. While the agreement between density-weighted PIV data and hot-wire measurements is not quite as tight as in the $\alpha = 10°$ case, the trends are still quite similar. "Self-correcting" the PIV velocity data by weighting the velocity with the density field obtained by the "pressure-from-PIV" method seems to provide the best agreement with the values obtained by hot-wire measurement, showing remarkable similarity throughout the interaction. The profiles which utilize CFD-based density data also follow the general trends of the directly-measured mass flux data. Here, the choice of turbulence model has a larger effect on the level of agreement with the density field generated using the SST-V model providing mass flux profiles which match the hot-wire data considerably better. In either case, the agreement is quite good when considering the tendency for small changes in interaction scale between the PIV and CFD fields to cause large discrepancies in computed parameters in regions of high gradient. The most conspicuous difference between the profiles is seen near the separated region, where the hot-wire data exhibits higher values. This is likely an artifact of the local mass flux value falling below the range over of the wire's aerodynamic calibration. Because these calibrations are carried out in situ using the incoming boundary layer of the wind tunnel, the lower limit on the range of mass flux values the probe is subjected to is constrained by how closely the wire can be brought to the wall surface. In practice, it is difficult to obtain velocities much below the sonic value in the Reynolds number range being explored here. With this noted caveat, the level of agreement displayed in the profiles implies that the hot-wire and PIV datasets are in congruence overall.

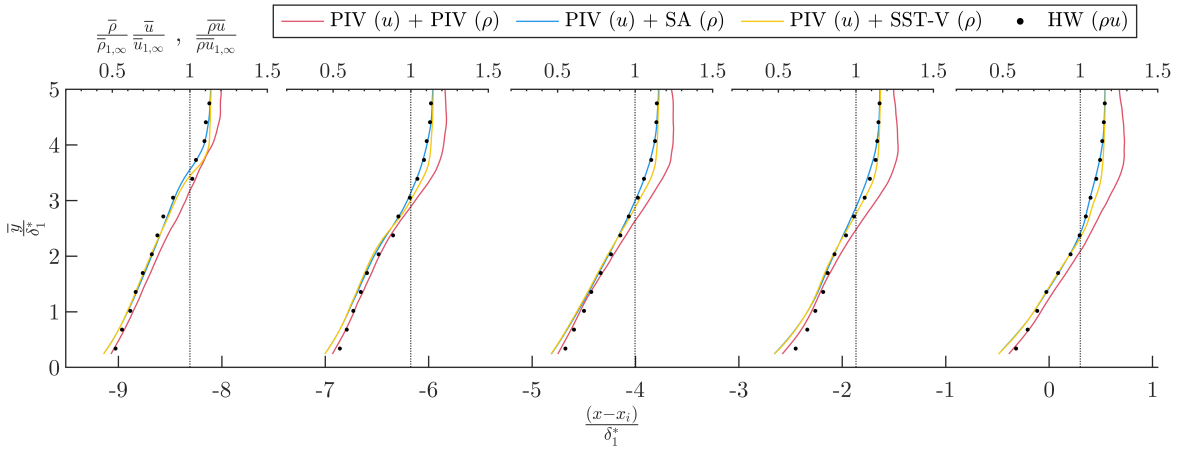
The superior agreement when applying the SST-V solution's density field stems from the fact that the SST-V model tends to generate a mean velocity field which better matches the PIV result. Relative performance of the two turbulence models in matching the PIV velocity data is shown in Fig. 18 where wall-normal profiles are compared at the same sampling stations as shown in the previous plots (for more global comparisons of turbulence models on this problem, see Ref. 12). Here, the clear difference between the two models is that the SST-V model predicts a larger upstream influence of the interaction, which better matches what is observed in the measurements. This trend is agnostic of the solver used, as evidenced by the additional data which is included from a solution which utilized the VULCAN-CFD solver. This does not necessarily constitute an endorsement of the SST-V model for separated flows, as it has been shown to over-estimate separation length in stronger interactions [34].

To further illustrate the relative differences in the weighting applied to the velocity data, Fig. 19 presents the density profiles derived from the PIV data against those from the RANS CFD. It is clear that CFD solutions and the PIV-derived density field show similar qualitative behavior, which is quite remarkable given the assumptions required. It is apparent from close inspection of the profiles that the PIV-derived density tends to under-predict the jump through the impinging and reflected shock waves. In fact, the agreement observed in Fig. 17 becomes all the more surprising when considering the neglection of compressible turbulence (ρ' terms in the derivation of Eq. (17)).

The difference between the profiles shown in Figs. 16b and 17 can be further analyzed by including the density-velocity correlation term, $\overline{\rho' u'}$. This may be computed from the hot-wire measurements if the density field is provided



(a)



(b)

Fig. 16 Mean axial velocity and mass flux in the $\alpha = 10°$ interaction at hot-wire survey stations. (a) Direct comparison of measured quantities and (b) corrected by mean density profile from CFD solution.

or inferred from turbulent Mach number values derived from PIV data if the assumptions inherent in the SRA can extended into the interaction region (dubious).

Direct comparison of axial turbulence intensity from PIV and hot-wire measurements within the interaction is affected by the same issues as in the incoming boundary layer. Here, the mean static pressure (density) field is an additional unknown. There exist two methods for bridging between the measurements, each requiring its own set of assumptions about the flow behavior. The first avenue is to attempt to compute mass flux fluctuation intensities from the PIV data. This involves carrying the SRA assumptions (derived for zero pressure gradient boundary layers) through the interaction region in addition to requiring mean density information which is not directly measured. The second method involves leveraging density information from an external source and applying the steps described in Section III.B.1 to the hot-wire data and separate the fluctuating intensity in density, velocity, and their cross-correlation. This requires continuing the assumption of the vorticity mode dominating the turbulence behavior, which becomes increasingly dubious in the post-shock region.

By dissecting the individual terms which make up the Reynolds stress transport equations, it becomes clear that several terms which are typically neglected in boundary layer flows may become significant in the presence of strong dilatation or high levels of pressure fluctuation. For example, the pressure "diffusion", $-\frac{\partial}{\partial x_k}\left(\overline{p'u_i''}\delta_{jk} + \overline{p'u_j''}\delta_{ik}\right)$, and

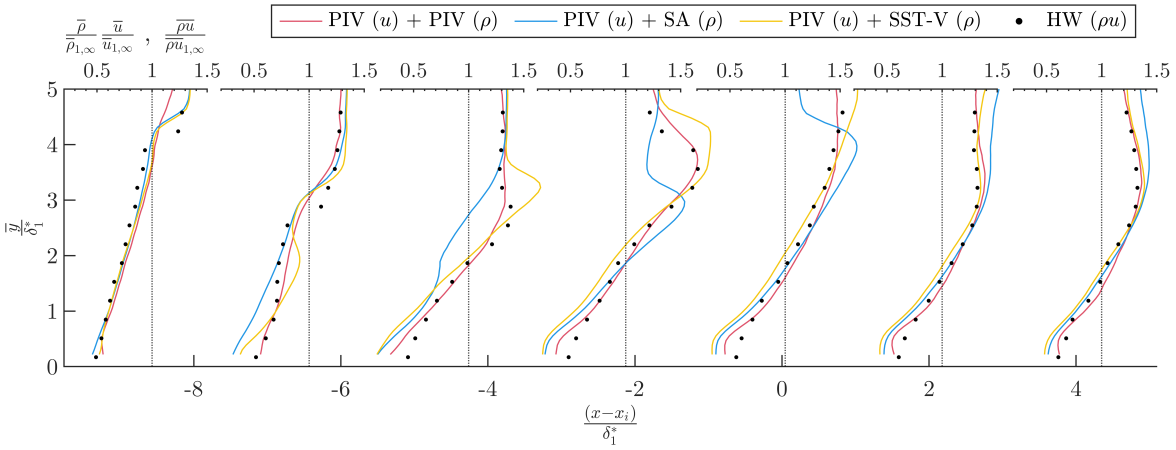


Fig. 17 Mean axial mass flux in the $\alpha = 16°$ interaction at hot-wire survey stations.

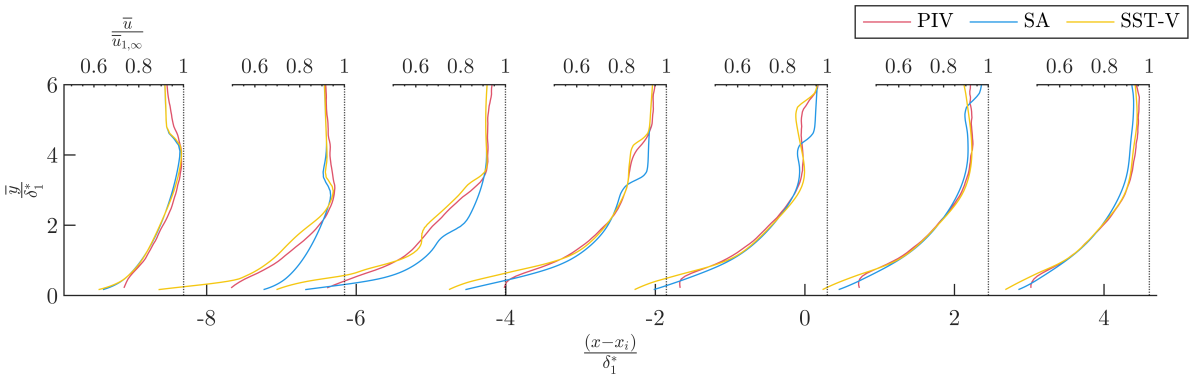


Fig. 18 Mean axial velocity in the $\alpha = 16°$ interaction at hot-wire survey stations.

"redistribution", $\overline{p'\left(\frac{\partial u_i''}{\partial x_j} + \frac{\partial u_j''}{\partial x_i} - \frac{2}{3}\frac{\partial u_k''}{\partial x_k}\delta_{ij}\right)}$, terms, which are sometimes neglected in Reynolds Stress Modeling (RSM) techniques, have been shown to be key to accurately predicting the re-attachment of separated shock-wave/boundary-layer interactions [35]. These terms, as well as the turbulent mass flux term, $\overline{u_i''}\left(\frac{\partial \bar{\tau}_{jk}}{\partial x_k} - \frac{\partial \bar{p}}{\partial x_j}\right) + \overline{u_j''}\left(\frac{\partial \bar{\tau}_{ik}}{\partial x_k} - \frac{\partial \bar{p}}{\partial x_i}\right)$, were identified to have a prominent role in the transport and redistribution of the turbulent energy in the region where the shear layer interacts with the impinging shock [36]. The terms involving cross-correlations of pressure and velocity are experimentally unavailable while evaluating the mass flux terms requires accurate collocated data for the mean pressure field and 2nd derivative of the velocity field. However, the comparison of the turbulence distribution within the current dataset with CFD solutions utilizing second-moment closures or large-eddy simulation (LES) is an area ripe for further exploration. This is beyond the scope of this work.

Applying Eq. (24) to the PIV data requires the assumption of a density-velocity correlation coefficient ($R_{\rho' u'}$) which is not known within the interaction. For this analysis, the value was chosen to be uniformly 1 for the current analysis to follow the original SRA proposed by Morkovin [25] and also simulate the case of strongest-possible density fluctuations originating from the vorticity mode of turbulence. Similarly, the assumption of constant mean total temperature is wrapped within the computation of the mean density field from PIV data. It is clear when dissecting Eq. (22), that a high level of correlation between density and velocity can drive significant mass flux fluctuations through the 2nd term in brackets. This can occur even at low $\overline{M}$ where the intensity of density fluctuations becomes less important, as in the highly turbulent region just above the separation zone in the $\alpha = 16°$ interaction.

Figure 20 shows a comparison of the resulting mass flux fluctuation profiles derived from the application of strong Reynolds analogy assumptions on the PIV data with those obtained directly with hot-wire measurements. In the $\alpha = 10°$

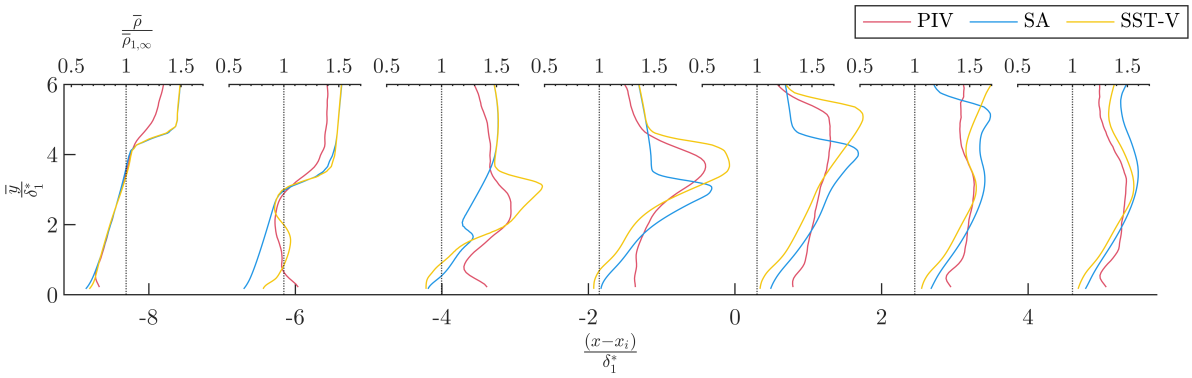


Fig. 19 Mean density in the $\alpha = 16°$ interaction at hot-wire survey stations.

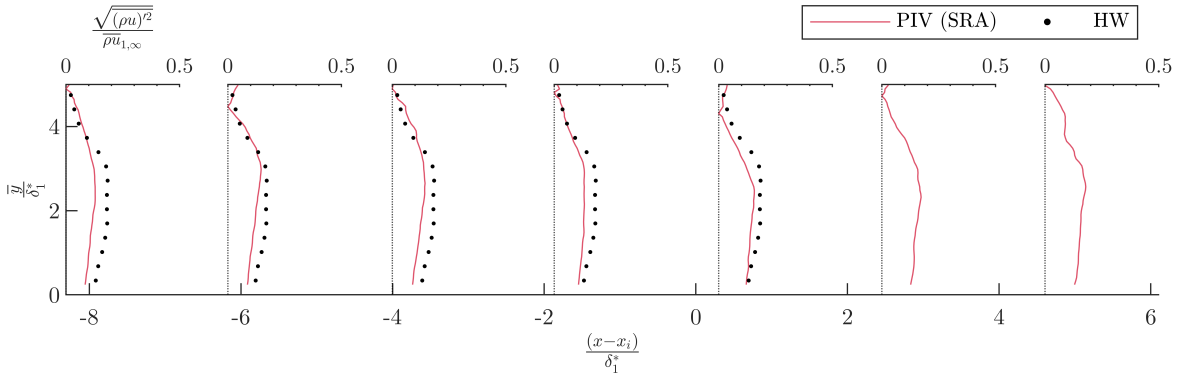
interaction, the intensity of mass flux fluctuations derived from the PIV data agree generally in magnitude to those from hot-wire. This agreement suggests that the measurements are in congruence and the SRA relationships are still accurate in this mildly perturbed boundary layer. Similarly, the most upstream profiles in the $\alpha = 16°$ are in alignment, the first being essentially an undisturbed turbulent boundary layer and the second being just aft of the mean reflected shock foot but still upstream of the strongest turbulent activity. Further downstream, data from the different measurements diverge markedly. In particular, the mass flux fluctuations as quantified by hot-wire measurement are significantly higher than what the PIV data and SRA would imply. This does not necessarily imply a mismatch in the measurements, but could simply be an artifact of the SRA breaking down. Specifically, the pressure fluctuations inherent to the interaction strain the assumption of negligible turbulence in the acoustic mode and the premise of constant density-velocity correlation coefficient has no physical support within the interaction. Since RANS solutions do not contain information on the density fluctuations, they cannot provide mass flux fluctuation information without invoking similar assumptions to those applied to the PIV and thus are not helpful in this context.

The fluctuation intensity in the PIV-derived velocity away from the wall is magnified away from the wall in a similar fashion to the upstream boundary layer when presented in Morkovin-scaled units, as in Fig. 12 of Ref. 9. Here, the values are not only amplified by the mean density variation (see Fig. 19) but also the high local Mach number, which incurs a high amplification of the velocity fluctuations stemming from compressibility.

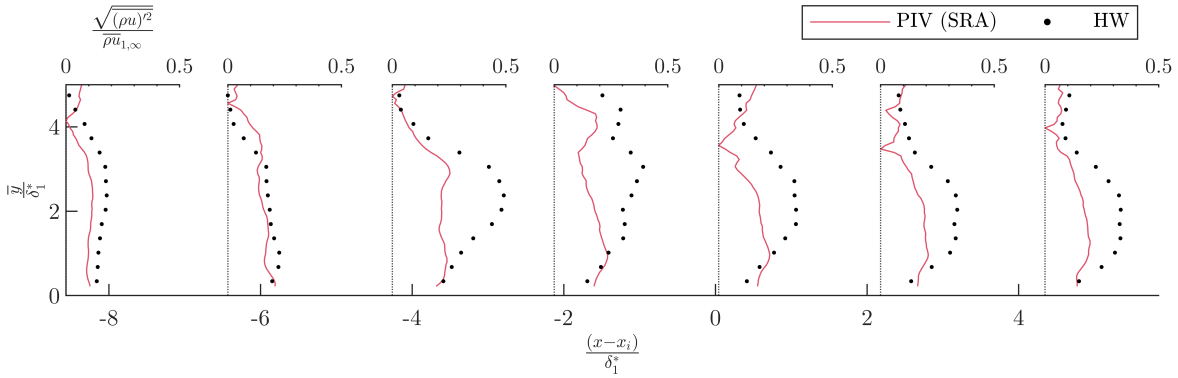
Deriving velocity and density fluctuation intensity values from the hot-wire data is possible if energy in the acoustic mode of the turbulence field is assumed small relative to the vorticity and entropy modes [37]. Confidence in this assertion is high in the incoming boundary layer but wanes in the interaction region. The collapse of this relation is three-fold. First, the impinging and reflected shock waves inject significant energy in to the acoustic mode [38]. Also, external pressure gradients, such as those applied by these waves, can induce compressible turbulence in boundary layer flows [26, 39, 40]. This strains the assumption of low turbulence Mach number which is synonymous with a solenoidal turbulence pattern. This is particularly true in the separated interaction, where strong velocity fluctuations are induced near the reflected shock foot and in the shear layer. Additionally, the unsteady motion of the shock waves (and separation bubble, if present) generates a strong amplification of the pressure fluctuations [41]. Nevertheless, the hot-wire data was reduced under the assumption of negligible pressure fluctuations to assess the error incurred by carrying this analysis through the interaction as a counterpart to the SRA-based correction of the PIV data, which contained more restrictive assumptions. Namely, the additional degree of freedom granted by variable density-velocity correlation was postulated to facilitate better agreement between the data.

Figure 21 shows the velocity turbulence levels directly from PIV in comparison with hot-wire data reduced as described as with values extracted from the CFD solutions . The fluctuations levels are normalized by the local mean velocity value to align with the direct output of the hot-wire measurement, which eliminates the additional uncertainty in ascertaining the local mean velocity from the hot-wire data. This also matches the normalization of Fig. 13. As in the incoming boundary layer data, the PIV data has been corrected using Eq. (21) to eliminate the additive measurement noise. Because the CFD solutions only compute the Favre-decomposed variables, the r.m.s. fluctuations provided are equivalent to

$$\frac{\widetilde{u''^2}}{\tilde{u}^2} = \frac{\overline{u'^2}}{\bar{u}^2} + \frac{\overline{\rho' u'^2}}{\bar{\rho}\bar{u}^2} - \frac{\left(\overline{\rho' u'}\right)^2}{\bar{\rho}^2\bar{u}^2} \tag{26}$$



(a)



(b)

Fig. 20 Turbulent mass flux estimated from applying the Strong Reynolds Analogy to PIV data in (a) the $\alpha = 10°$ and (b) the $\alpha = 16°$ interactions at hot-wire survey stations.

which contains similar terms but is not equivalent to the normalized mass flux fluctuation intensity (see Eq. (15)). The assumption made in making direct comparisons between $\overline{u'^2}$ and $\widetilde{u''^2}$ is that the higher order terms are negligible.

In Ref. 8, the normal components of the Reynolds stress were estimated from the reported TKE as $\widetilde{u''^2} \approx \frac{2}{3}\widetilde{k}$ by assuming the turbulent energy to be equally partitioned between the normal components. However, within the interaction region, the individual components can differ in regions of high strain. The individual turbulent stresses are available in CFD solutions utilizing two-equation models, such as the Menter SST-V in the form of $\tau_{ij}^t = -\overline{\rho}\widetilde{u_i''u_j''}$. This can be converted to velocity units as τ_{ij}^t/ρ which is equivalent to the Reynolds-averaged kinematic stresses when compressible turbulence can be neglected (see Appendix). For the one-equation SA model, the only turbulent stress directly computed is shear, which will be the only term compared to the measurements herein.

The magnitude of turbulent velocity fluctuations derived from hot-wire measurements exceeds that of the PIV and CFD through the majority of the interaction. Only outside the boundary layer and, in the $\alpha = 16°$ case , near the separated region do the PIV and CFD data approach or exceed the hot-wire values. This is not unexpected since the mass flux fluctuations being quantified with the hot-wire include density fluctuations in the aforementioned acoustic mode, the presence of which will be additive to the underlying vorticity mode turbulence being compared to in the PIV and CFD profiles. Near the separated region (near-wall portion of 2nd-5th profiles in Fig. 21b), the fluctuation levels become quite high in the PIV and CFD results due to the low local mean velocity. Because this increase is not reflected in the hot-wire data being referenced against, profiles of those two datasets are truncated at the axis limits. The lack of agreement in this region is likely due to the local mean mass flux falling below the range of the wire's aerodynamic calibration, as observed in Fig. 17, or the turbulence levels becoming too high to be accurately quantified by the hot-wire.

The axial component of velocity turbulence from CFD are also presented in Fig. 21 for comparison with the measurements. While this component appears to follow the qualitative behavior of the measurements, the CFD solutions exhibit distinctly lower values throughout the profiles. When observing the turbulence intensity in the other

2 components (not shown for brevity) it is clear that the PIV data exhibits more anisotropic behavior than the CFD solution, which acts much more like a pure shear flow.

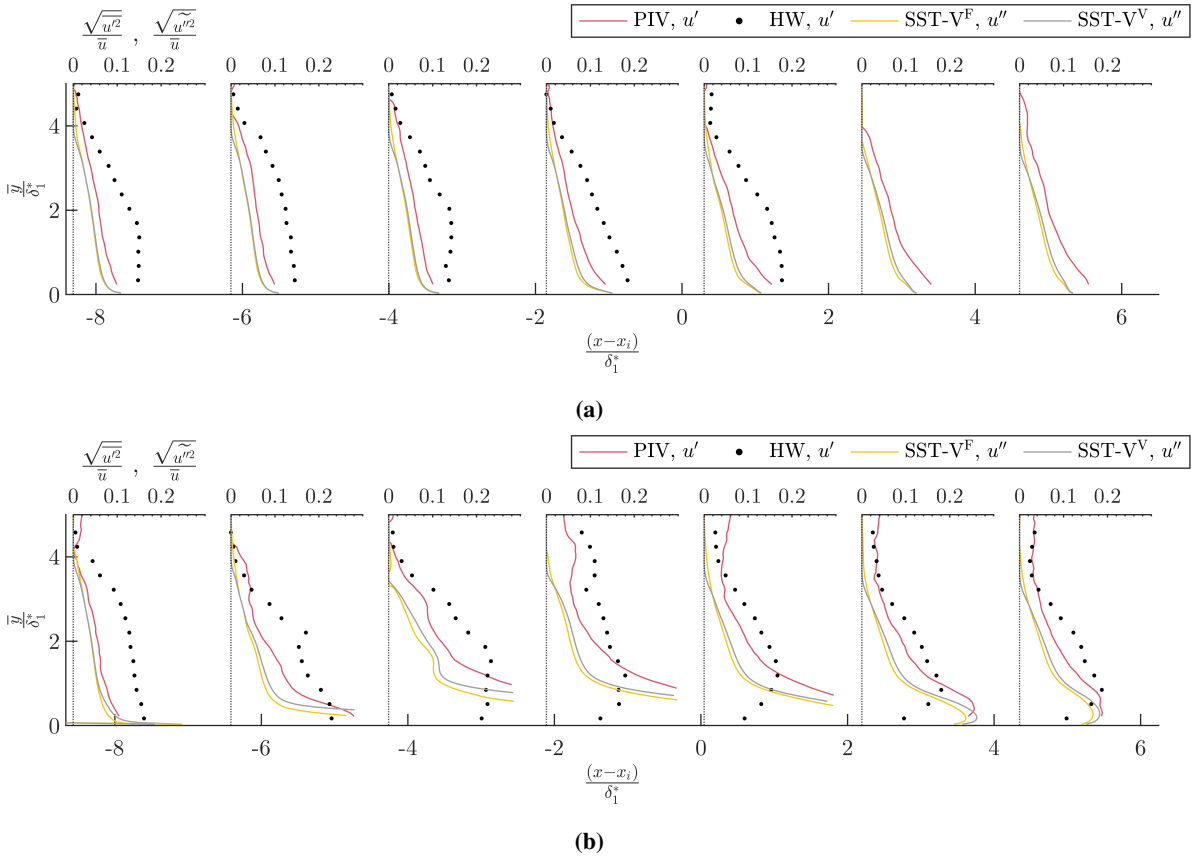


Fig. 21 Axial turbulence intensities from PIV, CFD, and estimates based on hot-wire measurements in (a) the $\alpha = 10°$ and (b) the $\alpha = 16°$ interactions. *Superscripts indicate CFD solver: "F" is FUN3D and "V" is VULCAN.*

The level of agreement between the measurements and simulations can be further analyzed through comparison of the TKE. Figure 22 shows profiles extracted at the hot-wire survey stations (identical to Fig. 21). At $\alpha = 10°$, the differences between CFD and measurements are quite small near the wall, with slightly higher turbulence observed in the VULCAN solution when compared to FUN3D. Away from the wall, the PIV shows a distinctly higher level of turbulence, which could stem from transient shock motion which is not captured by the RANS solutions. The same is true for the $\alpha = 16°$ case where the profiles from the reflected shock foot to the inviscid impingement point show higher peaks in the PIV. These are more closely followed by the VULCAN solution, but that trend reverses as the flow progresses downstream and the measured TKE decays to resemble the level predicted by FUN3D. For deeper analysis of code-to-code variations, see Ref. 12. Overall, it is clear that the SST-V turbulence model is performing much better in simulating the behavior of the TKE. The discrepancy between computational and experimental result seen in the axial turbulence is driven by the underlying Boussinesq approximation and its tendency toward equipartition of turbulent energy between the 3 components. This is a well-known shortcoming of the use of an isotropic eddy viscosity approach [42].

Finally, the primary shear stress, $\overline{u'v'}$, is plotted in Fig. 23. SA solutions are included in this figure since the shear stress rendered therein is physically relevant. In the more benign interaction at $\alpha = 10°$, the difference between CFD solutions is subtle, with SA predicting slightly stronger peak shear. All of the computational results show shear which exceeds that of the measurement, which is likely a result of the magnitude falling below the level which the PIV system can accurately quantify near the wall. At $\alpha = 16°$, the peak shear is much stronger. The VULCAN SST-V solution predicts the furthest upstream influence, as evidenced by the deviation in the furthest upstream profile while all other simulations results match the PIV in showing a relatively undisturbed linear shear profile. In the next several profiles,

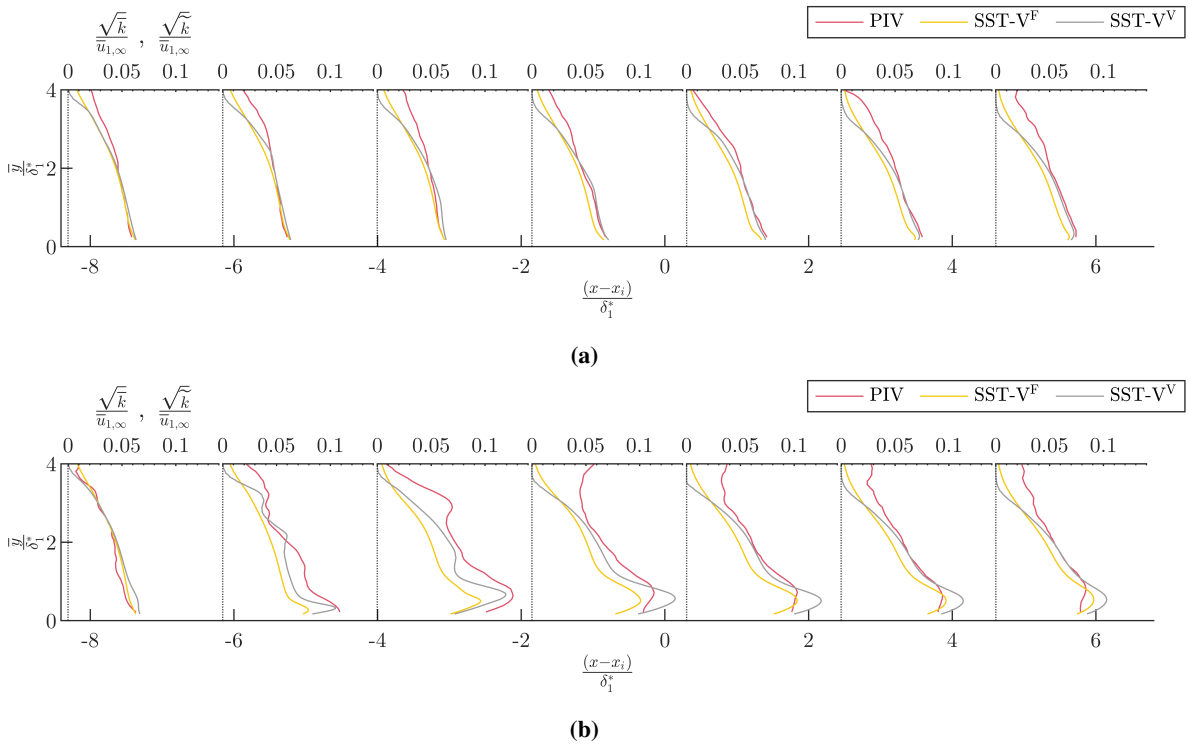


Fig. 22 Turbulent kinetic energy from PIV, CFD, and estimates based on hot-wire measurements in (a) the $\alpha = 10°$ and (b) the $\alpha = 16°$ interactions. *Superscripts indicate CFD solver: "F" is FUN3D and "V" is VULCAN.*

little can be gleaned from comparisons between the measurements and CFD due to strong effects of transient shock motion and variations in interaction scale. Additionally, it has been previously shown [9] that the PIV data exhibits a region near the reflected shock foot where the shear magnitude is significantly reduced and even reverses sign which has been observed in other [16]. This behavior is not observed in any of the CFD solutions (see contour plots in Ref. 12). By the inviscid impingement station, the profiles have settled to a similar behavior. The peak shear is initially higher in the simulations than experimental data, but relaxes to match more closely downstream. The FUN3D SST-V solution matches the PIV most closely in peak magnitude, while the SA solutions (which do not differ much between solvers) exhibit a peak location further from the wall which more closely matches the experimental result.

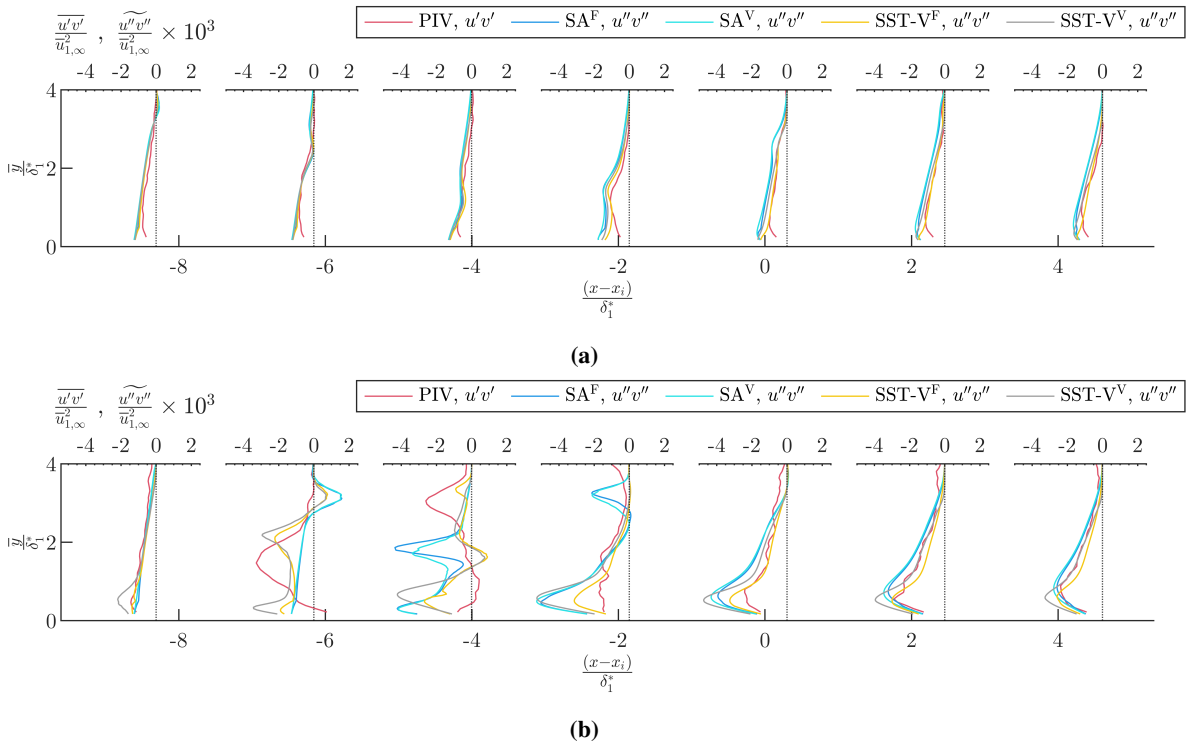


Fig. 23 In-plane shear turbulence from PIV, CFD, and estimates based on hot-wire measurements in (a) the $\alpha = 10°$ and (b) the $\alpha = 16°$ interactions. *Superscripts indicate CFD solver: "F" is FUN3D and "V" is VULCAN.*

3. Recovery Region

The data downstream of the primary interaction region is broken out in this section to allow for more detailed plotting of the data within each domain. Additionally, this region is delimited by having only Pitot probe data available to compare the PIV against, as hot-wire surveys were performed only in a tight spatial region near the shock impingement. Thus, the comparisons in this section are limited to comparisons between Pitot probe surveys, PIV data, and CFD solutions. As in Section III.B.2, data obtained by various RANS methods will be utilized to bridge between the distinct measured quantities.

Pitot pressures derived using the pressure-from-PIV method and CFD simulations are compared with probe measurements in Fig. 24. As in the interaction region, there is general concurrence in the profiles with a tendency for the PIV-derived data to exceed the probe values at the boundary layer edge in the unseparated case and do just the opposite in the separated interaction. This generally implies that the PIV-based values suggest lower and higher streamwise losses through the shock crossing which occurs near the boundary layer edge, respectively. This is a region where transient motion of the shock waves are significant and could be affecting the mean values extracted with both the probe- and laser-based methods. Still, the agreement is quite good considering the integrated nature of the pressure-from-PIV solution and the assumptions incurred. This region of the flowfield downstream of the interaction is especially sensitive to the integration problem as it is evaluated last by the spatial marching scheme and is thus subject to any error in the data upstream. The near-wall behavior of the $\alpha = 16°$ interaction is evidence of the error induced by applying the inviscid equations through the separation bubble.

The CFD solutions also match the probe data quite closely. They tend to follow the values beyond the boundary layer nearly identically with only small departures within. For both the unseparated and separated cases, the SST-V turbulence model yields a higher Pitot pressure in the outer part of the boundary layer and a lower value in the inner. In the $\alpha = 10°$ case, both models exhibit values higher than the measurements, tending toward the trend seen in the pressure-from-PIV profiles. Near the wall, the trend reverses and the CFD values fall below the probe data. For the $\alpha = 16°$ case, both models match the data quite well throughout, with a small advantage noted for the SST-V model at the upstream-most station which reverses to an advantage for SA as we progress downstream.

For further validation of the PIV measurements, velocity turbulence intensity data is extracted as wall-normal

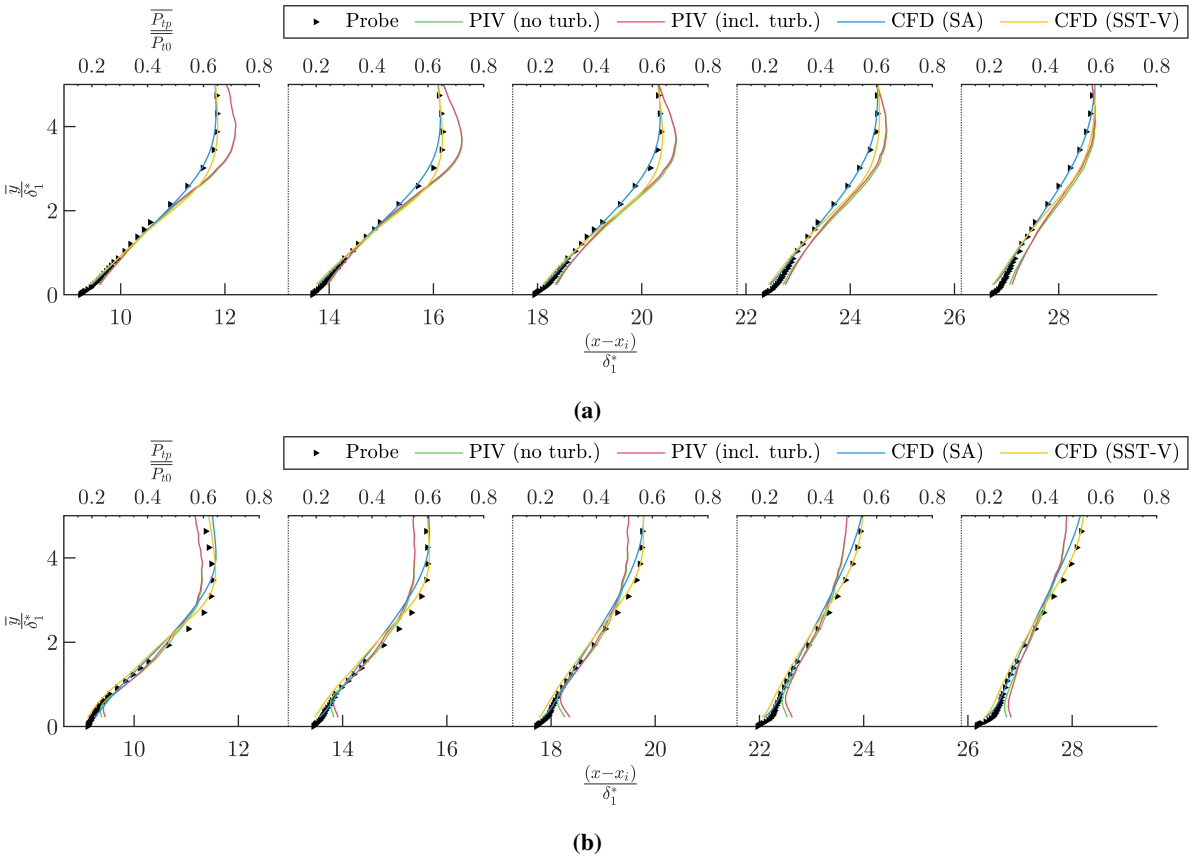


Fig. 24 Pitot pressure measurements in the recovery region for the (a) $\alpha = 10°$ and (b) $\alpha = 16°$ cases.

profiles at flow stations corresponding to the Pitot measurements. Here, the only comparison is with CFD solutions. The turbulent kinetic energy, k, is an instructive comparison since it is the primary element of the normal Reynolds stresses in this region of minimal normal strain. Inspection of the TKE instead of a particular normal stress component will also remove the differences between measurements and CFD solutions observed in Fig. 22 which stems from anisotropic behavior which is not accurately captured by the CFD. Figure 25 shows the PIV data and CFD result at the same probe stations as in Fig. 24. Generally, the RANS solutions are observed to match qualitatively with the behavior of the PIV profiles.

The $\alpha = 10°$ profiles show that the SA solution matches very closely with the PIV throughout this region. Within each profile, the SA solution tends to show the same peak intensity, peak location, and decay with wall distance as the measurements. Only in the aft-most profile does the PIV data show a nearly constant offset to higher turbulence intensity which happens to peak at a value which matches more closely with the SST-V solutions. The near-match in profile shape even at this station is still noteworthy. The SST-V solutions show a distinctly lower level of turbulence through the outer region of the boundary layer and only begin to approach the measurement value for $y/\delta_1^* < 1.5$. This agreement is much better in the SST-V solution generated using the VULCAN-CFD package than FUN3D in the more upstream profiles. As the flow progresses downstream, the two converge to be nearly identical except for the more abrupt decrease in turbulence exhibited by the VULCAN solution as the freestream is approached.

In the $\alpha = 16°$ case, peak k is higher than the measurement for all 3 CFD examples at the upstream-most station, but the SA solution rapidly evolves to match closely with the PIV data after a few stations. The wall-normal distance at which peak TKE occurs is also closely matched for the SA model, with the SST-V solution featuring a peak closer to the wall. As in the unseparated case, the SA profiles tend to exhibit a larger wall-normal extent with significant energy.

As in the turbulence plotted in Section III.B.2, the PIV displays elevated levels of turbulence away from the wall relative to the CFD prediction. Here, however, the turbulent energy outside the boundary layer are expected to be elevated due to turbulence production by the shock waves and it is likely that the CFD is under-predicting the turbulence

at large distances from the wall in at least the first few stations.

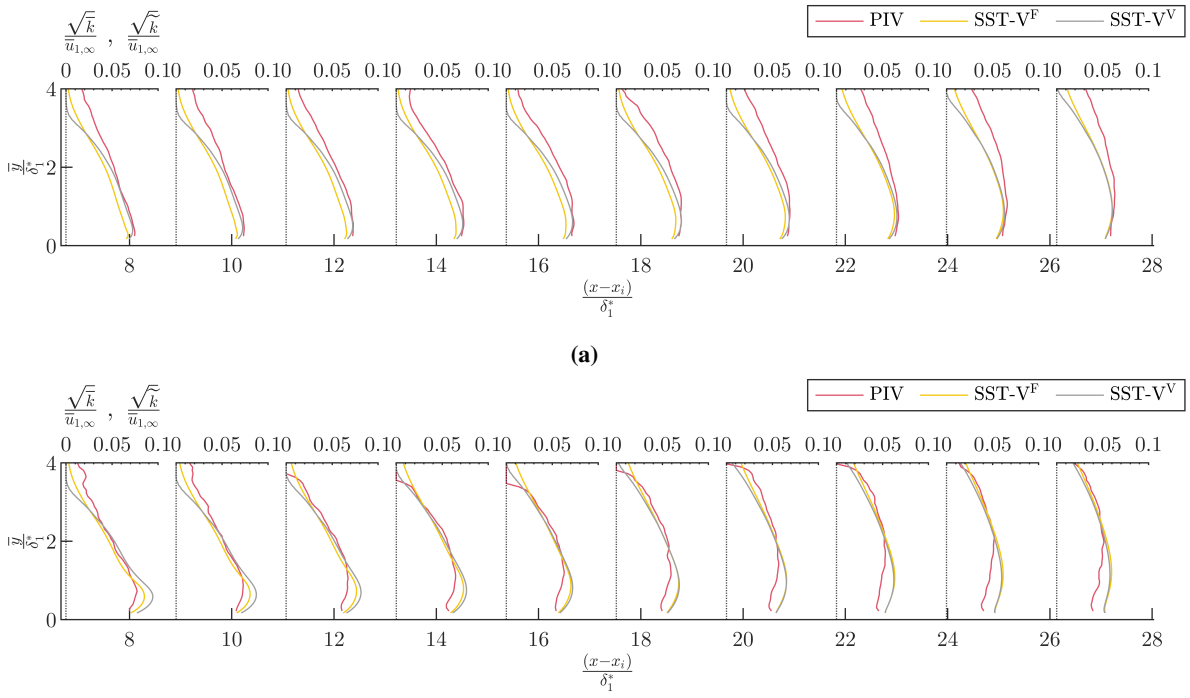


Fig. 25 Turbulent kinetic energy from PIV and CFD in the recovery region of (a) the $\alpha = 10°$ and (b) the $\alpha = 16°$ interactions. *Superscripts indicate flow solver package: "F" is FUN3D and "V" is VULCAN.*

Similarly, the turbulent shear stress in this region agrees quite well between the PIV and RANS CFD. As shown in Fig. 26, the peak magnitude is universally higher in the CFD than the measurement at the most upstream station, which follows from what was observed at the downstream end of Fig. 23. In the $\alpha = 10°$ case, the profiles collapse to quite similar behavior just a few stations further downstream. The $\alpha = 16°$ case exhibits a bit more variation among the CFD solutions with the SST-V model generating stronger peak shear, which occurs closer to the wall than the peak of the SA profile. It is also notable that the peak dissipates more rapidly with downstream distance in the RANS solutions than in the PIV data. The tendency for measured shear stress to exceed solutions using the SST model in this type of flow has been attributed to the shear stress limiter value [34].

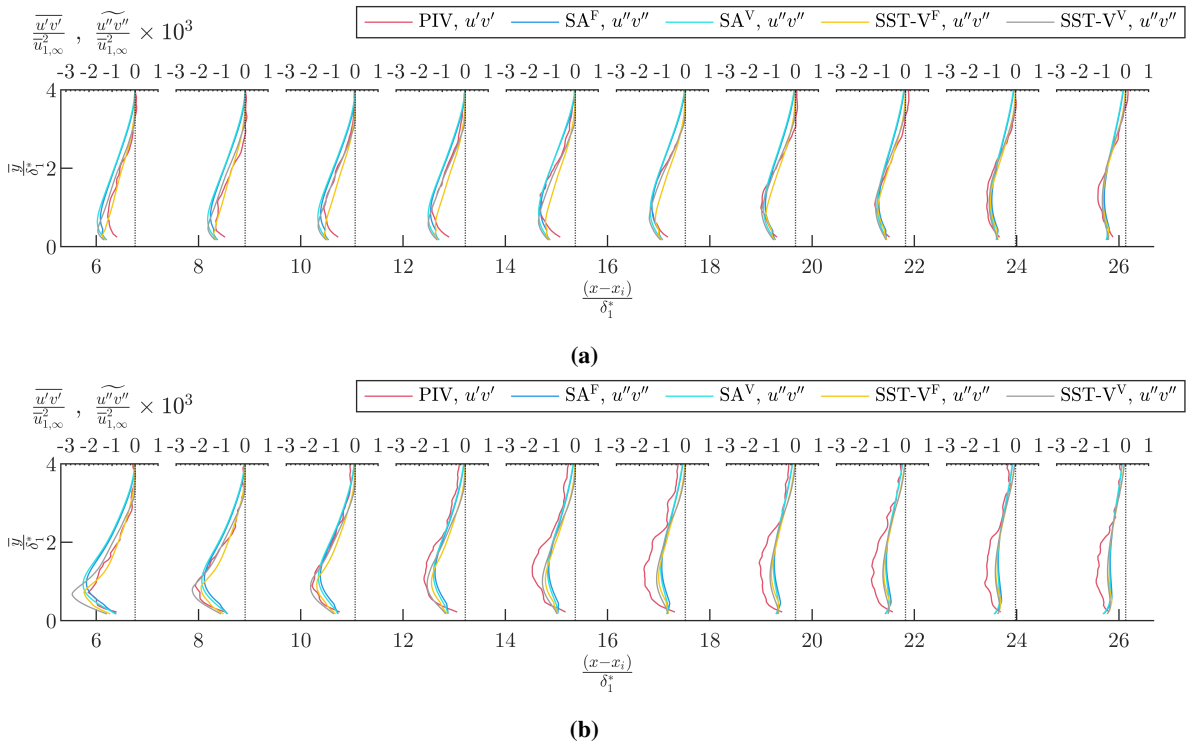


Fig. 26 In-plane shear turbulence from PIV compared with CFD in the recovery region of (a) the $\alpha = 10°$ and (b) the $\alpha = 16°$ interactions. *Superscripts indicate flow solver package: "F" is FUN3D and "V" is VULCAN.*

IV. Conclusions

This paper presents detailed comparisons of the various measurements contained in the Mach 2.5 2D shock-wave/boundary-layer dataset. Congruence of the measured data in both the incoming boundary layer velocity as well as various quantities within and beyond the interaction was confirmed. This implies not only accuracy in the measurands, but also in the spatial registration of the various data despite the significant intervals of time and wind tunnel disassembly/reassembly required between their acquisition. Inferences as to the relative accuracy of the various measurement techniques were made to inform users of the dataset as to which may be best-suited to a particular portion of the flowfield. In this way, the various measurements can be used synergistically to provide the best-possible experimental survey of the flowfield behavior.

In order to make connections between measurements which did not quantify identical flow properties, several methods were applied. Mean thermodynamic properties were estimated directly from 3D velocity data using the method proposed by van Oudheusden [24] which expanded the common "pressure-from-PIV" method to compressible and shock-containing flows. The data derived therewith exhibited considerable agreement with the probe data, especially considering the crudeness of the spatial integration technique. RANS CFD solutions were also leveraged as a comparison point and also a source for thermodynamic properties within the interaction flowfield. The measured flowfield was found to be best represented by solutions utilizing the Menter SST-V model.

In the region within and downstream of the interaction, the key difference observed between the CFD solutions and measured data lies in the turbulence behavior. The RANS-based solutions were all found to exhibit peak axial turbulence intensities below that of the PIV, which exhibited a more anisotropic behavior. In the far field, this discrepancy faded and the measurements and CFD come into consensus. Within the interaction region, the only turbulent measurements available for comparison with CFD come from PIV since the turbulence models applied do not compute a mass flux fluctuation intensity which could be directly contrasted with the hot-wire results. Attempts to bridge between these measurements using Strong Reynolds Analogy assumptions yielded favorable comparisons for the weaker interaction, but failed in the separated interaction. This is expected as the presence of static pressure fluctuations invalidates the SRA. Future scale-resolving simulations and measurements at higher freestream Mach number may further elucidate the behavior of density-velocity coupling in this region.

Appendix

Mean turbulent mass flux

By definition, the Reynolds average of a Favre velocity fluctuation is directly related to the density-velocity correlation by expanding the definition given in Eq. (3) as

$$\begin{aligned}\frac{\overline{\rho u_i''}}{\overline{\rho}} &= 0\\ \overline{\rho}\,\overline{u_i''} + \overline{\rho' u_i''} &= 0\\ \overline{u_i''} &= -\frac{\overline{\rho' u_i''}}{\overline{\rho}}\,.\end{aligned}$$

When also considering the property that $u_i'' = u_i' + \overline{u_i''}$, it becomes clear that the density-velocity correlation is identical whether using Favre or Reynolds versions of the fluctuation. These terms quantify the effect of compressibility and have been included in alternatives to the linear Boussinesq eddy viscosity model [43]. While not directly measurable, values can be obtained through combined measurements of velocity, density, and mass flux fluctuation levels or through assumptions such as the SRA.

Reynolds stress term expansion

The Reynolds stress terms are defined using Favre-averaged fluctuations in CFD solvers for mathematical convenience. These can be expanded into their Reynolds-averaged components by expanding Eq. (9) to the form

$$-\tau_{ij}^t \equiv \overline{\rho}\widetilde{u_i'' u_j''} = \overline{\rho}\,\overline{u_i' u_j'} + \bar{u}_i\overline{\rho' u_j'} + \bar{u}_j\overline{\rho' u_i'} + \overline{\rho' u_i' u_j'} - \frac{\overline{\rho' u_i'}\;\overline{\rho' u_j'}}{\overline{\rho}}\,.$$

Here one can see how $\tau_{ij}^t/\rho \approx \overline{u_i' u_j'}$ in incompressible flows or compressible mean flow where significant density fluctuations are not present. Turbulent boundary layer flows are a prime example of this type of behavior, where SRA-based analyses (Eq. (19)) suggest that the magnitude of $\overline{\rho' u_i'}$ remains insignificant for freestream Mach numbers well above 1.

Hot-wire response to non-axial flow

In a flow of arbitrary direction, the response of the hot-wire probe deviates from the typical one-dimensional analysis typically applied to interpret the recorded signal of a single-normal wire ($U = \overline{u} + u'$, $V = 0$, $W = 0$). The inclusion of additional mean velocity (introduced by misalignment of the local flow direction and the probe axis) and turbulence intensity components is considered here. This will provide a quantitative estimate of the error in attributing the observed mean and fluctuating signal all to the axial component.

In wire-oriented coordinates, the response to mass flux in each direction can be taken from the analysis of inclined hot-wires in incompressible flows,

$$E/S_{\rho U} = \left(Q_N^2 + k^2 Q_T^2 + h^2 Q_B^2\right)^{1/2}\,,$$

where the subscripts, N, T, and B represent the probe normal, tangential, and binormal directions, respectively [44, 45]. In the current context, the Q variable will be treated as a mass flux instead of a velocity, as it is in incompressible flows. If we apply the "cosine law" and assume that the wire is insensitive to tangential mass flux ($k = 0$) and also define the probe axis to be aligned with the tunnel axis, $\vec{x}$, and the wire axis with $\vec{z}$, then the voltage signal can be related to flow variables in test facility coordinates as

$$\begin{aligned}E/S_{\rho U} &= \left\{\left[\overline{\rho u} + (\rho u)'\right]^2 + h^2\left[\overline{\rho v} + (\rho v)'\right]^2\right\}^{1/2}\\ &= \overline{\rho u}\left[1 + 2\frac{(\rho u)'}{\overline{\rho u}} + \frac{(\rho u)'^2}{\overline{\rho u}^2} + h^2\left(\frac{\overline{\rho v}}{\overline{\rho u}}\right)^2 + 2h^2\frac{(\rho v)'\,\overline{\rho v}}{\overline{\rho u}^2} + h^2\frac{(\rho v)'^2}{\overline{\rho u}^2}\right]^{1/2}\,.\end{aligned}$$

The relation may be linearized using the binomial expansion ($(1+\epsilon)^{1/2} = 1 + \frac{1}{2}\epsilon + \frac{1}{8}\epsilon^2 + ...$ for $\epsilon \ll 1$) in order to facilitate the separation of the mean and fluctuating components of this signal. This results in the expression

$$\frac{E}{S_{\rho U}} = \overline{\rho u}\left[1 + \frac{(\rho u)'}{\overline{\rho u}} + \frac{1}{2}\frac{(\rho u)'^2}{\overline{\rho u}^2} + \frac{1}{2}h^2\left(\frac{\overline{\rho v}}{\overline{\rho u}}\right)^2 + h^2\frac{(\rho v)'\,\overline{\rho v}}{\overline{\rho u}^2} + \frac{1}{2}h^2\frac{(\rho v)'^2}{\overline{\rho u}^2}\right] + H.O.T..$$

The time-average signal can then be expressed as

$$\frac{\overline{E}}{S_{\rho U}} = \overline{\rho u}\left\{1 + \frac{1}{2}\left[h^2\left(\frac{\overline{\rho v}}{\overline{\rho u}}\right)^2 + \frac{\overline{(\rho u)'^2}}{\overline{\rho u}^2} + h^2\frac{\overline{(\rho v)'^2}}{\overline{\rho u}^2}\right]\right\}$$

and the fluctuating signal about this mean is

$$\frac{E'}{S_{\rho U}} = (\rho u)' + h^2\frac{\overline{\rho v}}{\overline{\rho u}}(\rho v)' + H.O.T..$$

This can be squared and time-averaged to relate the level of voltage fluctuation to the turbulent stresses as

$$\begin{aligned}\frac{\overline{E'^2}}{S_{\rho U}^2} &= \overline{(\rho u)'^2} + 2h^2\frac{\overline{\rho v}}{\overline{\rho u}}\overline{(\rho u)'(\rho v)'} + h^4\left(\frac{\overline{\rho v}}{\overline{\rho u}}\right)^2\overline{(\rho v)'^2} \\ &= \bar{\rho}^2\left[\overline{u'^2} + 2h^2\frac{\overline{\rho v}}{\overline{\rho u}}\overline{u'v'} + h^4\left(\frac{\overline{\rho v}}{\overline{\rho u}}\right)^2\overline{v'^2}\right] + \\ &\overline{\rho'^2}\left[\bar{u}^2 + 2h^2\frac{\overline{\rho v}}{\overline{\rho u}}\bar{u}\bar{v} + h^4\left(\frac{\overline{\rho v}}{\overline{\rho u}}\right)^2\bar{v}^2\right] + \\ &2\left[\bar{\rho}\bar{u}\left(\overline{\rho' u'} + h^2\frac{\overline{\rho v}}{\overline{\rho u}}\overline{\rho' v'}\right) + \bar{\rho}\bar{v}\left(h^2\frac{\overline{\rho v}}{\overline{\rho u}}\overline{\rho' u'} + h^4\left(\frac{\overline{\rho v}}{\overline{\rho u}}\right)^2\overline{\rho' v'}\right)\right] + H.O.T.\end{aligned}$$

which, under closer inspection, aligns with the notion that the hot-wire response to mass flux fluctuations is dominated by the axial component as long as the local flow angle and binormal turbulence intensity remain small.

Eddy Viscosity Estimates

Eddy viscosity, the modeled variable by which the Navier-Stokes equations are closed in the RANS solutions, can be inferred from PIV data since it contains both turbulence intensities and mean velocity gradient information. As discussed, this can only be practically achieved through the shear stress component as

$$\nu_t \approx \frac{-\overline{u'v'}}{\frac{\partial \bar{u}}{\partial y} + \frac{\partial \bar{v}}{\partial x}} \tag{27}$$

where the kinematic stresses are substituted for the Favre-averaged versions which appear in the RANS equations.

However, there are several error sources which must be acknowledged when applying this method. First, the measured velocity fields contain noise, which becomes especially problematic when taking spatial derivatives of the mean velocity field, but also pollutes the local turbulent stress. This can be somewhat alleviated by employing image filtering techniques which remove noise while preserving features, such as the median filter. The second issue is that the variable by which we are evaluating the result is derived from two essentially independent measurands, so errors in each combine additively in the final result. Finally, the individual measurements contained within a PIV vector field are not necessarily constrained to follow either continuity or logical turbulence decay, so they are likely to stray further from the physical truth. With this in mind, the broad behavior of the eddy viscosity field is examined in comparison with the RANS turbulence models previously presented.

Figure 27 shows this for PIV datasets from two different test entries in comparison with results from the one-equation Spalart-Allmaras model as well as Menter's SST-V method. The region of high eddy viscosity roughly tracing the reflected shock which appears in both PIV datasets is an artifact of shock motion which will not be captured by any RANS solution and can be ignored in this comparison. The high values which appear near the wall can also be

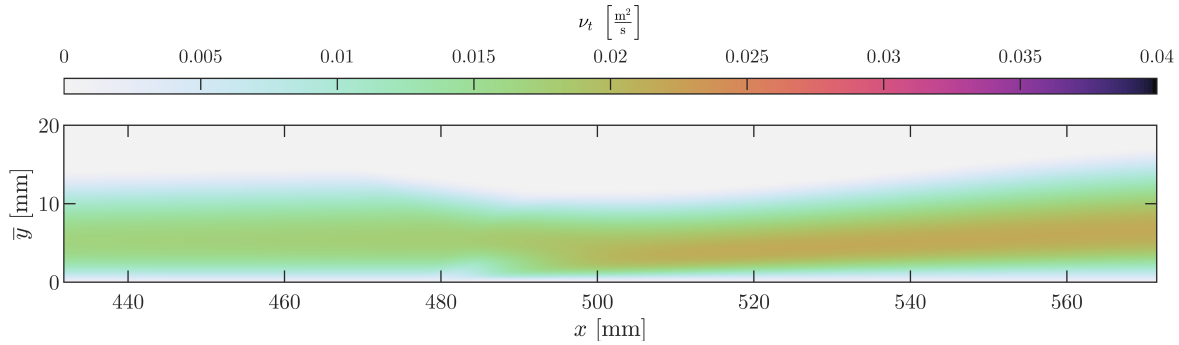
disregarded as they are a non-physical result of the PIV measurement being unable to resolve the velocity gradient very near the wall. The PIV results show the same qualitative behavior as the CFD solution with nearly constant value in the incoming boundary layer, a decrease within the interaction region, and then an increase beyond the incoming boundary layer value in the recovery region with a wall-normal spreading. Generally, the SA model predicts the eddy viscosity to be more broadly distributed in the wall-normal direction with a similar level of increase in the recovery region downstream of the interaction. The SST-V solution generally exhibits a lower level of eddy viscosity through the interaction, exhibiting a sharp decrease where the boundary layer encounters the reflected shock foot. This is due to the action of the shear stress limiter, as discussed previously.

The measurements from the 2022 dataset exhibit a reduced level of Reynolds shear stress in the incoming boundary layer which was noted in Ref. 9. The contemporary data appears to match the CFD and canonical flat plate boundary layer behavior, but exhibits higher values in the recovering boundary layer. The propensity for shock separated flows to demonstrate turbulent shear stress levels beyond the shear stress limiter used in the Menter SST model has been noted in previous investigations[34]. It does appear that the dataset which better captures the peak turbulent shear stress (Fig. 27d) exhibits a bifurcated pattern similar to the behavior of the SST-V solution in Fig. 27b.

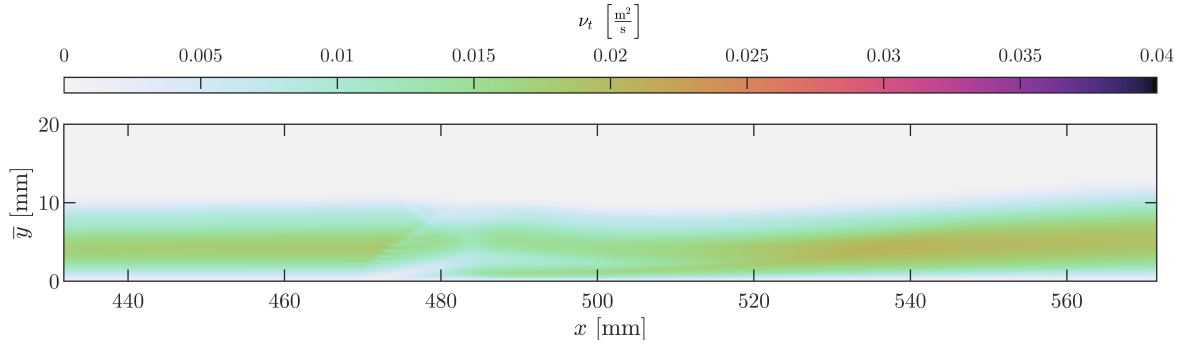
Even for a large statistical sample of the velocity field by conventional standards (1000 vector maps) and a 7×7 median filtering of the velocity gradient and turbulent stress fields, both measurement sets feature small-scale variations which are driven by noise in the turbulent stress value. This can only be resolved with increased sampling which would take advantage of the ergodicity of the turbulence and mean flow. Additionally, the downward-looking PIV arrangement necessitated by the test section geometry is not optimized for this type of detailed investigation of near-wall behavior. An increase in magnification could possibly better resolve both the turbulence and mean velocity fields in this region. This would require only a change to the imaging arrangement since the minimum interframe time capability of the system is not yet being approached. However, this would only be possible with a concurrent de-scoping of the spatial coverage of the measurements, as the reduced axial coverage would necessitate a prohibitive number of imaging stations to cover the entire extent shown here. This is being considered for a possible follow-on test entry.

Acknowledgments

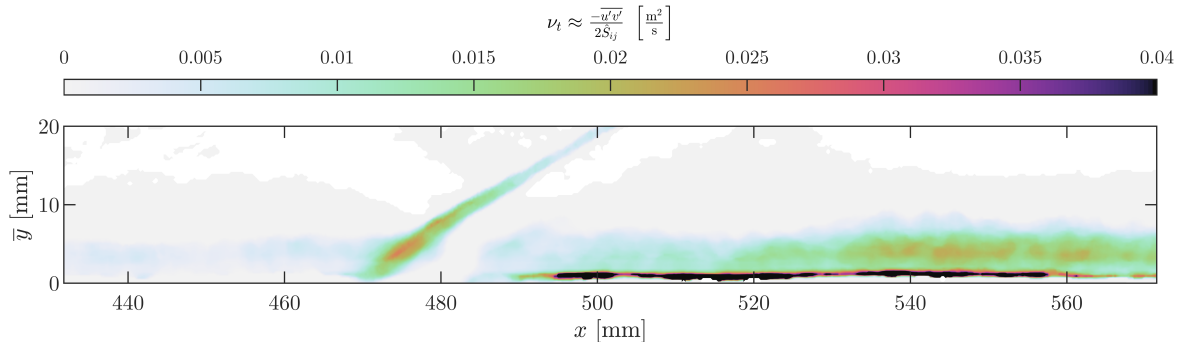
This research is sponsored by the NASA Transformational Tools and Technologies (TTT) Project of the Transformative Aeronautics Concepts Program under the Aeronautics Research Mission Directorate.



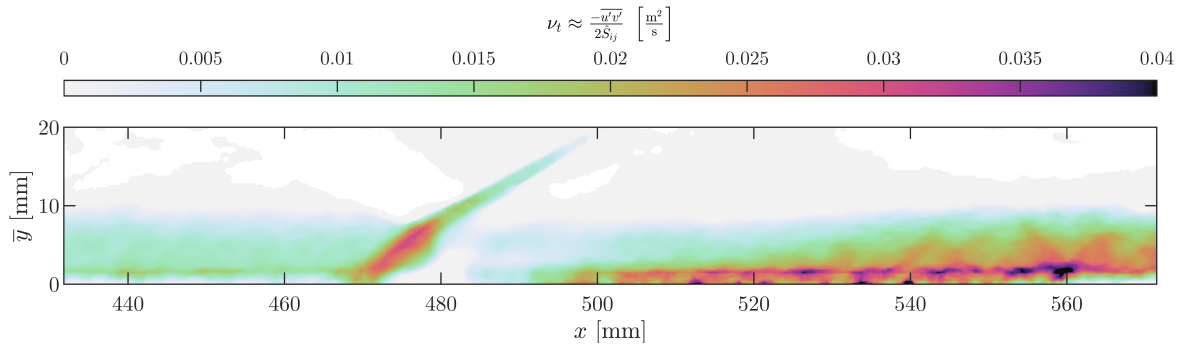
(a) VULCAN-CFD, SA model



(b) VULCAN-CFD, SST-V model



(c) 2022 PIV measurement



(d) 2024 PIV measurement

Fig. 27 Eddy viscosity values from the VULCAN solution utilizing the SA model (a-b) in comparison with estimates from PIV measurements (c-d) in the $\alpha = 16°$ interactions

References

[1] DeBonis, J. R., Oberkampf, W. L., Wolf, R. T., Orkwis, P. D., Turner, M. G., Babinsky, H., and Benek, J. A., "Assessment of Computational Fluid Dynamics and Experimental Data for Shock Boundary-Layer Interactions," *AIAA Journal*, Vol. 50, No. 4, 2012, pp. 891–903. doi:10.2514/1.J051341.

[2] Settles, G. S., and Dodson, L. J., "Supersonic and hypersonic shock/boundary-layer interaction database," *AIAA Journal*, Vol. 32, No. 7, 1994, pp. 1377–1383. doi:10.2514/3.12205.

[3] Aeschliman, D. P., and Oberkampf, W. L., "Experimental Methodology for Computational Fluid Dynamics Code Validation," *AIAA Journal*, Vol. 36, No. 5, 1998, pp. 733–741. doi:10.2514/2.461.

[4] Babinsky, H., Oorebeek, J., and Cottingham, T., "Corner effects in reflecting oblique shock-wave/boundary-layer interactions," *51st AIAA Aerospace Sciences Meeting including the New Horizons Forum and Aerospace Exposition*, 2013, pp. 1–11. doi:10.2514/6.2013-859.

[5] Garnier, E., "Stimulated detached eddy simulation of three-dimensional shock/boundary layer interaction," *Shock Waves*, Vol. 19, No. 6, 2009, pp. 479–486. doi:10.1007/s00193-009-0233-7.

[6] Davis, D. O., "CFD Validation Experiment of a Mach 2.5 Axisymmetric Shock-Wave/Boundary-Layer Interaction," *Proceedings of the ASME/JSMA/KSME 2015 Joint Fluids Engineering Conference*, Fluids Engineering Division Summer Meeting, Vol. Volume 1: Symposia, 2015. doi:10.1115/AJKFluids20156342, v001T06A001.

[7] Sasson, J., "Conical Shock Wave Turbulent Boundary Layer Interactions in a Circular Test Section at Mach 2.5," Ph.D. thesis, Case Western Reserve University, 2022. URL http://rave.ohiolink.edu/etdc/view?acc_num=case1648825433614363.

[8] Sasson, J., Reising, H. H., Davis, D. O., and Barnhart, P. J., "Summary of Shock Wave Turbulent Boundary Layer Interaction Experiments In a Circular Test Section," *AIAA SciTech 2023*, 2023. doi:10.2514/6.2023-0442.

[9] Reising, H. H., and Davis, D. O., "PIV Measurements of Shock-Wave/Boundary-Layer Interactions at Mach 2.5 in a Circular Test Section," *AIAA SCITECH 2024 Forum*, American Institute of Aeronautics and Astronautics, 2024. doi:10.2514/6.2024-2554.

[10] Comte-Bellot, G., and Sarma, G., "Constant Voltage Anemometer Practice in Supersonic Flows," *AIAA Journal*, Vol. 39, No. 2, 2001, pp. 261–269. doi:10.2514/2.1321.

[11] Reising, H. H., and Davis, D. O., "Development and Assessment of a New Particle Image Velocimetry System in the NASA GRC 225 cm^2 Wind Tunnel," *AIAA SciTech 2023*, National Harbor, MD, 2023. doi:10.2514/6.2023-0631.

[12] Friedlander, D. J., Georgiadis, N. J., Howerton, L. W., and Reising, H. H., "Numerical Simulations of an Axisymmetric Shock-Wave/Boundary-Layer Interaction," *AIAA SciTech 2025 Forum*, 2025.

[13] Chue, S., "Pressure probes for fluid measurement," *Progress in Aerospace Sciences*, Vol. 16, No. 2, 1975, pp. 147–223. doi:10.1016/0376-0421(75)90014-7.

[14] Walz, A., *Boundary layers of flow and temperature*, M.I.T. Press, 1969.

[15] Whitfield, D. L., and High, M. D., "Velocity-Temperature Relations in Turbulent Boundary Layers with Nonunity Prandtl Numbers," *AIAA Journal*, Vol. 15, No. 3, 1977, pp. 431–434. doi:10.2514/3.60637.

[16] Humble, R. A., Scarano, F., and Van Oudheusden, B. W., "Particle image velocimetry measurements of a shock wave/turbulent boundary layer interaction," *Experiments in Fluids*, Vol. 43, No. 2-3, 2007, pp. 173–183. doi:10.1007/s00348-007-0337-8.

[17] Kovásnay, L. S. G., "The Hot-Wire Anemometer in Supersonic Flow," *Journal of the Aeronautical Sciences*, Vol. 17, No. 9, 1950, pp. 565–572. doi:10.2514/8.1725.

[18] Webster, C. A. G., "A note on the sensitivity to yaw of a hot-wire anemometer," *Journal of Fluid Mechanics*, Vol. 13, No. 02, 1962, p. 307. doi:10.1017/s0022112062000695.

[19] Smits, A. J., and Muck, K. C., "Constant Temperature Hot-Wire Anemomenter Practice in Supersonic Flows - Part : The Inclined Wire," *Experiments in Fluids*, Vol. 2, 1984, pp. 33–41.

[20] Ligrani, P. M., and Bradshaw, P., "Spatial resolution and measurement of turbulence in the viscous sublayer using subminiature hot-wire probes," *Experiments in Fluids*, Vol. 5, No. 6, 1987, pp. 407–417. doi:10.1007/bf00264405.

[21] Hutchins, N., Nickels, T. B., Marusic, I., and Chong, M. S., "Hot-wire spatial resolution issues in wall-bounded turbulence," *Journal of Fluid Mechanics*, Vol. 635, 2009, pp. 103–136. doi:10.1017/s0022112009007721.

[22] Cameron, J. D., Morris, S. C., Bailey, S., and Smits, A. J., "Effects of hot-wire length on the measurement of turbulent spectra in anisotropic flows," *Measurement Science and Technology*, Vol. 21, No. 10, 2010, p. 105407. doi:10.1088/0957-0233/21/10/105407.

[23] Mosele, J.-P., Gross, A., and Slater, J., "Numerical Investigation of Asymmetric Mach 2.5 Turbulent Shock Wave Boundary Layer Interaction," *Aerospace*, Vol. 10, No. 5, 2023, p. 417. doi:10.3390/aerospace10050417.

[24] van Oudheusden, B. W., "Principles and application of velocimetry-based planar pressure imaging in compressible flows with shocks," *Experiments in Fluids*, Vol. 45, No. 4, 2008, pp. 657–674. doi:10.1007/s00348-008-0546-9.

[25] Morkovin, M. V., "Effects of compressibility on turbulent flows," *Mécanique de la Turbulence*, Vol. 367, No. 380, 1962, p. 26.

[26] Smits, A. J., and Dussauge, J.-P., *Turbulent Shear Layers in Supersonic Flow*, 2006.

[27] Smits, A. J., "Wall-wake laws for the mean velocity and the turbulence," *Journal of Fluid Mechanics*, Vol. 989, 2024. doi:10.1017/jfm.2024.519.

[28] Gaviglio, J., "Reynolds analogies and experimental study of heat transfer in the supersonic boundary layer," *International Journal of Heat and Mass Transfer*, Vol. 30, No. 5, 1987, pp. 911–926. doi:10.1016/0017-9310(87)90010-x.

[29] Huang, P. G., Coleman, G. N., and Bradshaw, P., "Compressible turbulent channel flows: DNS results and modelling," *Journal of Fluid Mechanics*, Vol. 305, 1995, pp. 185–218. doi:10.1017/s0022112095004599.

[30] Guarini, S. E., Moser, R. D., Shariff, K., and Wrary, A., "Direct numerical simulation of a supersonic turbulent boundary layer at Mach 2.5," *Journal of Fluid Mechanics*, Vol. 414, 2000, pp. 1–33. doi:10.1017/s0022112000008466.

[31] Zhang, Y.-s., Bi, W.-t., Hussain, F., and She, Z.-s., "A generalized Reynolds analogy for compressible wall-bounded turbulent flows," *Journal of Fluid Mechanics*, Vol. 739, 2014, pp. 392–420. doi:10.1017/jfm.2013.620.

[32] Kistler, A. L., "Fluctuation Measurements in a Supersonic Turbulent Boundary Layer," *The Physics of Fluids*, Vol. 290, No. 2, 1959. doi:10.1063/1.1705925.

[33] Martin, M. P., "Direct numerical simulation of hypersonic turbulent boundary layers. Part 1. Initialization and comparison with experiments," *Journal of Fluid Mechanics*, Vol. 570, 2007, pp. 347–364. doi:10.1017/S0022112006003107.

[34] Georgiadis, N., and Yoder, D., "Recalibration of the Shear Stress Transport Model to Improve Calculation of Shock Separated Flows," *51st AIAA Aerospace Sciences Meeting including the New Horizons Forum and Aerospace Exposition*, American Institute of Aeronautics and Astronautics, 2013. doi:10.2514/6.2013-685.

[35] Gerolymos, G. A., Lo, C., Vallet, I., and Younis, B. A., "Term-by-Term Analysis of Near-Wall Second-Moment Closures," *AIAA Journal*, Vol. 50, No. 12, 2012, pp. 2848–2864. doi:10.2514/1.j051654.

[36] Vyas, M. A., Yoder, D. A., and Gaitonde, D. V., "Reynolds-Stress Budgets in an Impinging Shock-Wave/Boundary-Layer Interaction," *AIAA Journal*, Vol. 57, No. 11, 2019, pp. 4698–4714. doi:10.2514/1.j058487.

[37] Kovásnay, L. S. G., "Turbulence in Supersonic Flow," *Journal of the Aeronautical Sciences*, Vol. 20, No. 10, 1953, pp. 657–674. doi:10.2514/8.2793.

[38] Ribner, H., "Shock-turbulence interaction and the generation of noise," Tech. rep., NACA TN 3255, 1954.

[39] Lele, S. K., "Compressibility Effects on Turbulence," *Annual Review of Fluid Mechanics*, Vol. 26, No. 1, 1994, pp. 211–254. doi:10.1146/annurev.fl.26.010194.001235.

[40] Andreopoulos, Y., Agui, J. H., and Briassulis, G., "Shock Wave—Turbulence Interactions," *Annual Review of Fluid Mechanics*, Vol. 32, No. 1, 2000, pp. 309–345. doi:10.1146/annurev.fluid.32.1.309.

[41] Fang, J., Zheltovodov, A. A., Yao, Y., Moulinec, C., and Emerson, D. R., "On the turbulence amplification in shock-wave/turbulent boundary layer interaction," *Journal of Fluid Mechanics*, Vol. 897, 2020. doi:10.1017/jfm.2020.350.

[42] Pope, S. B., "A more general effective-viscosity hypothesis," *Journal of Fluid Mechanics*, Vol. 72, No. 02, 1975, p. 331. doi:10.1017/s0022112075003382.

[43] Taulbee, D., and VanOsdol, J., "Modeling turbulent compressible flows - The mass fluctuating velocity and squared density," *29th Aerospace Sciences Meeting*, American Institute of Aeronautics and Astronautics, 1991. doi:10.2514/6.1991-524.

[44] Hinze, J. O., *Turbulence*, McGraw Hill, 1959.

[45] Acrivlellis, M., "Hot-wire signal analyses," *Journal of Physics E: Scientific Instruments*, Vol. 15, No. 3, 1982, pp. 289–297. doi:10.1088/0022-3735/15/3/012.